Development of Efficiently Coupled Fluid-Flow/Geomechanics Model To Predict Stress Evolution in Unconventional Reservoirs With Complex-Fracture Geometry

Anusarn Sangnimnuan, Jiawei Li, and **Kan Wu,** Texas A&M University

Summary

Stress changes associated with reservoir depletion are often observed in the field. Stress evolution within and surrounding drainage areas can greatly affect further reservoir developments, such as completion of infill wells and refracturing. Previous studies mainly focus on biwing planar-fracture geometry, which limits the possibility of investigating stress evolution caused by complex-fracture geometry. In this paper, we have developed a novel and efficient coupled fluid-flow/geomechanics model with an embedding-discrete-fracture model (EDFM) to characterize stress evolution associated with depletion in unconventional reservoirs with complex-fracture geometry. Coupled geomechanics/fluid flow was developed using the well-known fixed-stress-split method, which is unconditionally stable and computationally efficient to simulate how stress changes during reservoir depletion. EDFM was coupled to the model to gain capability of simulating complex-fracture geometries using structured grids. The model was validated against the classical Terzaghi (1925) and Mandel (1953) problems. Local grid refinement was used as a benchmark when comparing results from EDFM for fractures with 0 and 45° angles of inclination. After that, the model was used to analyze stress distribution and reorientation in reservoirs with three different fracture geometries: planar-fracture (90° angle of inclination), 60° inclination, and nonplanar-fracture geometries. As the pressure decreases, reservoir stresses tend to change anisotropically depending on depletion area. The principal stress parallel to the initial fracture reduces faster than the orthogonal one as a function of time. The decrease rate of principal stresses is distinct for different shapes of depleted areas created by different fracture geometries. The rectangular shape produced by the planar-fracture geometry yields the largest stress-reorientation area for a variety of differential-stress (DS) values (difference between two horizontal principal stresses). The squared shape produced by nonplanar-fracture geometry yields stress reorientation only for low DS. The results indicate that created fracture geometry has a significant effect on stress distribution and reorientation induced by depletion. To the best of our knowledge, this is the first time a coupled fluid-flow/geomechanics model incorporated with EDFM has been developed to efficiently calculate stress evolution in reservoirs with complex-fracture geometry. Characterization of stress evolution will provide critical guidelines for optimization of completion designs and further reservoir development.

Introduction

Stress changes associated with reservoir depletion have been considered as an important parameter when studying fracture propagation for applications such as infill wells or refracturing. Gupta et al. (2012) studied the connection between reservoir depletion and stress distribution and found that the smaller the DS, the more likely it was for stress to reorient. Roussel et al. (2013) confirmed this phenomenon by studying stress evolution in the infill-well region, showing longitude fractures generated in the infill well. However, stress can reverse back to its original orientation after a certain period of production time. Safari et al. (2015) showed that fractures created by infill wells can curve because of stress reorientation in the field from tightly spaced horizontal wells. It was concluded that production from infill wells can be maximized by minimizing communication between wells, which can be achieved by studying how stress evolution occurs in the field because of reservoir depletion, and optimizing fracture spacing.

To accurately predict stress evolution caused by reservoir depletion, a coupled model of fluid flow and geomechanics that is capable of predicting stress change caused by the poroelastic effect is necessary. There are two types of models: a fully coupled method and a sequentially implicit method. The sequentially implicit method solves fluid flow and geomechanics separately during the same timestep and produces a smaller system of equations, resulting in lower computational time compared with the fully coupled method. As discussed by Kim et al. (2011a, 2011b, 2011c, 2013), the sequential method can mainly be divided into two main categories: solving geomechanics first or solving fluid flow first. Both methods can yield either the same result or different results, depending on the type of problem being solved. However, among the methods mentioned by Kim et al. (2011a), the fixed-stress-split method is found to be unconditionally stable. This method was also used by Jha and Juanes (2014) to simulate multiphase flow and geomechanics of faulted reservoirs. Wang (2014) also used this fixed-stress-split method to develop a reservoir simulator capable of simulating a complex coupled poromechanical process on massively parallel computers.

There are many types of numerical methods that can model coupled fluid flow/geomechanics. The finite-element method (FEM) is one such method used in many commercial software products because of its capability in solving solid mechanics equations. Simulators used by both Roussel et al. (2013) and Gupta et al. (2012) are dependent on the FEM. However, as presented by Tang et al. (2015), the finite-volume method (FVM), which has mainly been used in computational fluid dynamics, can be a good alternative to FEM with its capability of handling both linear and nonlinear continuum solid mechanics (Jasak et al. 2000). A main feature of FVM is its solutions with cell-centered bases, whereas FEM handles only solutions at the edges of elements. Tang et al. (2015) adapted FVM using Open Source Field Operation and Manipulation (OpenFOAM) to model coupled poroelastoplasticity. The model contains both material

Original SPE manuscript received for review 10 May 2017. Revised manuscript received for review 28 July 2017. Paper (SPE 189452) peer approved 14 September 2017.

nonlinearity and strong solid/fluid-coupling effects derived from implicit/explicit discretization. The developed model yields good agreement with analytical solutions.

Although much work has been performed to investigate stress evolution caused by reservoir depletion (Gupta et al. 2012; Roussel et al. 2013; Safari et al. 2015), one main feature that is still missing is complexity of fracture geometry. Previous studies only focus on planar-fracture geometry, which is not always the case in the field, especially for unconventional reservoirs. Therefore, incorporating complex-fracture geometries in the model can yield a more-accurate result in terms of stress analysis and production forecast as actual fracture geometry in the field is being analyzed. Complex-fracture geometries can be obtained using a fracture-propagation model. In many circumstances, complex-fracture geometries are modeled through unstructured grids with grid refinement around fractures (Cipolla et al. 2011). However, this comes with high computational cost and instability in some cases. Li and Lee (2008) originally developed a method called the EDFM. Xu (2015) further developed this model and incorporated EDFM into commercial simulators. The main idea of EDFM is to use the structured-gridding discretization to explicitly model the influences of fractures through transmissibility between nonneighboring cells by the definition of nonneighboring connections. In EDFM, the reservoir is discretized with structured grids and additional grids are introduced for fractures. EDFM has been improved from the dual-porosity model (Bai 1999) by explicitly representing each fracture using an element or a control volume. EDFM is found to honor computational performance of structured grids as well as accuracy and flexibility of explicit-fracture modeling. Coupling EDFM with the coupled geomechanics/fluid-flow model allows the prediction of stress evolution in reservoirs with complex-fracture geometry using a structured-gridding system. This can be useful in terms of both computational time and accuracy. Ren et al. (2017) implemented EDFM to model fluid flow on their finite-element-base simulator (XFEM), mainly used for approximating geomechanics with a dual-porosity-hybrid model to handle small-scale fracture networks around primary fractures in stimulated reservoir volume regions.

In this study, our main goal is to address stress evolution induced by depletion in unconventional reservoirs with complex-fracture geometry, which is significantly important for infill-well treatments and refracturing. To achieve this, we have developed a 3D coupled geomechanics/fluid-flow model with EDFM. The model is dependent on an open source code, OpenFOAM using FVM. EDFM was implemented on the model, resulting in the fluid flow in matrix and fracture being solved implicitly to open the possibility of simulating complex-fracture geometry on the structured-gridding system, which is known to have high computational efficiency. The main advantage of our model is that it is able to simulate the effect of coupled geomechanics/fluid flow on complex-fracture geometry in a multiple-fracture system with high computational efficiency, which cannot be achieved by commercial software that requires an unstructured-gridding system, to forecast production and study stress evolution caused by the poroelastic effect. Details of the model are introduced in the next section.

Governing Equations

Coupled Fluid Flow/Geomechanics. Coupled fluid flow/geomechanics is derived from the Biot (1941, 1955) theory, which describes the poroelastic effect in isothermal linear isotropic poroelastic material, which can be used to model a reservoir. The governing equations for this coupled system come from mass conservation and linear-momentum balance. Mechanical deformation can be expressed as

$$\nabla \cdot \sigma + \rho_b g = 0, \tag{1}$$

where σ is the total stress tensor (Rank 2), ρ_b is single-phase fluid bulk density, and g is gravitational acceleration. Combined with the Biot (1941, 1955) theory, which relates fluid-pressure change to strain rate, the relationship between stress and strain with poroelastic effect from Kim et al. (2011b) can be written as

$$\sigma - \sigma_0 = C_{dr} : \varepsilon - b(p - p_0)I, \tag{2}$$

$$\frac{1}{M}\frac{\partial p}{\partial t} + b\frac{\partial \varepsilon_v}{\partial t} + \nabla \cdot V = q, \tag{3}$$

where the subscript 0 refers to reference state, C_{dr} is the Rank 4 elastic tensor, I is the Rank 2 identity tensor, p is fluid pressure, b is the Biot coefficient, and ε is the linearized strain tensor, which can be written in terms of displacement as

$$\varepsilon = \frac{1}{2}(\nabla u + \nabla^T u), \tag{4}$$

where $\varepsilon_v = tr(\varepsilon)$ is the volumetric strain, V is fluid-flow rate, q is a source/sink term, M is the Biot modulus, and u is the displacement vector containing three components. The relationship between the Biot modulus and the Biot coefficient can be shown as

$$\frac{1}{M} = \phi c_f + \frac{b - \phi}{K_s}, \tag{5}$$

$$b = 1 - \frac{K_{dr}}{K_s}, \tag{6}$$

where c_f is fluid compressibility, K_s is the bulk modulus of solid grain, ϕ is porosity, and K_{dr} is the drained bulk modulus, which can be computed from the drained rock properties, such as Young's modulus (E) and Poisson's ratio (ν). According to Kim et al. (2011b), K_{dr} can be chosen to achieve an optimal convergence rate for the fixed-stress iterative coupling:

$$K_{dr} = \frac{E(1 - v)}{(1 + v)(1 - 2v)}. \tag{7}$$

Volumetric mean total stress is the trace of the stress tensor $\left(\sigma_v = \frac{1}{3}tr\sigma\right)$. With the relationship between volumetric stress and strain, Eq. 2 can be rewritten as

$$(\sigma_v - \sigma_{v,0}) + b(p - p_0) = K_{dr}\varepsilon_v. \tag{8}$$

The fluid-flow rate can be written in terms of pressure through Darcy's law as

$$V = -\frac{k}{\mu_f}(\nabla p - \rho_b g), \tag{9}$$

where μ_f is fluid viscosity and k is matrix permeability (Rank 2 tensor). If we substitute Eq. 9 in Eq. 3, which represents the fluid-pressure change caused by the strain rate, and neglect the gravitational term, we have

$$\frac{1}{M}\frac{\partial p}{\partial t}+b\frac{\partial \varepsilon_v}{\partial t}-\frac{k}{\mu_f}(\nabla^2 p)=q. \quad (10)$$

Eqs. 2 and 10 are called fixed-strain split (Kim et al. 2011b), in which the equations are solved in terms of strain. Fixed-strain represents the sequential method in which geomechanics and fluid-flow equations are solved separately, starting by solving Eq. 10 and then Eq. 2 using the relationship in Eq. 1. The iteration stops when the convergence criteria are reached for both equations. As demonstrated by Kim et al. (2011a), this method is not stable for high coupling strength $\left(\tau=\frac{b^2 M}{K_{dr}}>1\right)$. Thus, Eq. 10 is modified by writing volumetric strain in terms of volumetric strength as

$$\left(\frac{1}{M}+\frac{b^2}{K_{dr}}\right)\frac{\partial p}{\partial t}+\frac{b}{K_{dr}}\frac{\partial \sigma_v}{\partial t}-\frac{k}{\mu_f}(\nabla^2 p)=q. \quad (11)$$

Eq. 11 is called the fixed-stress-split method and is unconditionally stable. K_{dr} can also be expressed in terms of the first and second Lamé constants (λ and μ) as

$$\mu=\frac{E}{2(1+v)}, \quad (12)$$

$$\lambda=\frac{vE}{(1+v)(1-2v)}. \quad (13)$$

If we substitute Eqs. 11, 12, 13, and 2 in Eq. 1 and neglect the gravitational term, we can finally obtain the relationship between displacements and pressure under the momentum-balance condition:

$$\nabla\cdot[\mu\nabla u+\mu\nabla u^T+\lambda I tr(\nabla u)]+\nabla\cdot\sigma_0-b\nabla p+b\nabla p_0=0. \quad (14)$$

Eq. 11 can also be written in terms of displacement as

$$\left(\frac{1}{M}+\frac{b^2}{K_{dr}}\right)\frac{\partial p^n}{\partial t}-\frac{b^2}{K_{dr}}\frac{\partial p^{n-1}}{\partial t}+b\frac{\partial(\nabla\cdot u)}{\partial t}-\frac{k}{\mu_f}(\nabla^2 p^n)=q, \quad (15)$$

where n is the current timestep and n–1 is the previous timestep. Eqs. 14 and 15 are solved through an iteration loop to obtain displacement and pressure as shown in **Fig. 1.** The details of discretization and how to solve each equation will be discussed in the Numerical Model section.

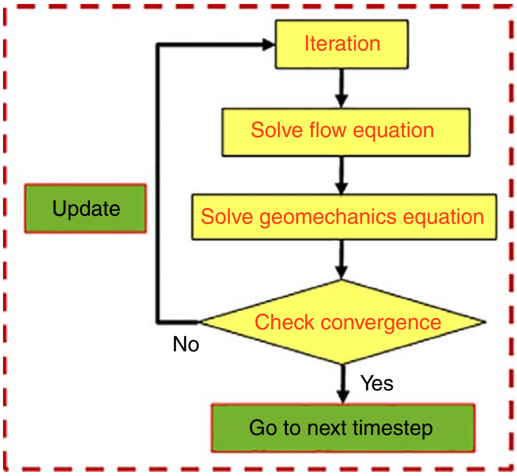

Fig. 1—Diagram showing fixed-stress method for fluid-flow and geomechanics.

Our model includes not only the zero-displacement boundary condition, but also the traction boundary condition for the geomechanics equation. For the traction boundary condition, displacements at boundaries are computed from the traction boundary and are then applied to solve for the entire displacement field. The traction boundary equation is obtained by setting Eq. 1 equal to the traction value rather than zero:

$$\nabla\cdot[\mu\nabla u+\mu\nabla u^T+\lambda I tr(\nabla u)]+\nabla\cdot\sigma_0-b\nabla p+b\nabla p_0=T, \quad (16)$$

where T is the traction at the boundaries.

Fully Coupled Fluid Flow/Geomechanics With EDFM. In this subsection, we implemented EDFM to our coupled model to efficiently simulate complex-fracture geometry without using unstructured grids. As mentioned by Xu et al. (2016) and Du et al. (2017), EDFM has been developed with the concept of honoring the accuracy of DFMs while keeping the efficiency offered by structured grids. The idea is to completely separate the fracture from the matrix domain and have them communicate through transmissibility. It is worth mentioning that deformation inside the fracture is not considered for EDFM, and deformations from the matrix (reservoir) and the fracture are combined. Both the fracture and matrix domains have the same grid size. The volume of the fracture segment (V_f) represented in the fracture domain can be computed as

$$V_f = S_{\mathrm{seg}} w_f, \quad (17)$$

where S_{seg} is the area of the fracture segment perpendicular to the fracture aperture and w_f is the fracture aperture. The pore volume of the fracture (ϕ_f) domain will be assigned as

$$\phi_f = \frac{S_{\mathrm{seg}} w_f}{V_b}, \quad (18)$$

where V_b is the bulk volume of the cell assigned to the fracture segment. The next important parameter is transmissibility, which represents the flow from the fracture to the matrix domain and can be defined as

$$q_{f-m} = \lambda_t T_{f-m} \Delta p, \quad (19)$$

where $q_{f\text{–}m}$ is the flow between the fracture and the matrix cell, λ_t is the relative mobility, $T_{f\text{–}m}$ is the transmissibility between the fracture and the matrix, and Δp is the pressure difference between the fracture and the matrix cell.

For connections between two fracture cells, as discussed by Xu et al. (2016), transmissibility can be expressed as

$$T_{f-f} = \frac{T_1 T_2}{T_1 + T_2}, \quad (20a)$$

$$T_1 = \frac{k_{f1} w_{f1} L_{\mathrm{int}}}{d_{f1}}, \quad T_2 = \frac{k_{f2} w_{f2} L_{\mathrm{int}}}{d_{f2}}, \quad (20b)$$

where $T_{f\text{–}f}$ is the transmissibility between Fracture Cells 1 (T_1) and 2 (T_2); k_{f1} and k_{f2} are the permeability inside Fracture Cells 1 and 2, respectively; w_{f1} and w_{f1} are the width of Fracture Cells 1 and 2, respectively; L_{int} is the length of the intersection line; and d_{f1} and d_{f2} are the weighted average of the normal distances from the centroids of the subsegments (on both sides) to the intersection line.

The transmissibility factor between the matrix and the fracture segment ($T_{f\text{–}m}$) depends on the matrix permeability and the fracture geometry. Eq. 20a can be modified incorporating the normal vector between the fracture and the matrix as

$$T_{f-m} = \frac{2A_f (\overline{\overline{K}} \cdot \vec{n}\,) \cdot \vec{n}}{d_{f-m}}, \quad (21)$$

where A_f is the area of the fracture segment on one side, $\overline{\overline{K}}$ is the matrix-permeability tensor, $\vec{n}$ is the normal vector of the fracture plane, and $d_{f\text{–}m}$ is the average normal distance from the matrix to the fracture, which can be calculated as

$$d_{f-m} = \frac{\int_V x_n \mathrm{d}V}{V_c}, \quad (22)$$

where x_n is the distance from the matrix to the fracture cell and V_c is the cell volume. The transmissibility term is then added to Eq. 15 to account for flow associated with the fracture as

$$\left(\frac{1}{M} + \frac{b^2}{K_{dr}}\right)\frac{\partial p^n}{\partial t} - \frac{b^2}{K_{dr}}\frac{\partial p^{n-1}}{\partial t} + b\frac{\partial(\nabla \cdot u)}{\partial t} - \frac{k}{\mu_f}(\nabla^2 p^n) + \lambda_t T_{f-m}({p_f}^n - p^n) = 0. \quad (23)$$

Similarly, the conservation in fracture can be written as

$$\left(\frac{1}{M_f} + \frac{b^2}{K_{dr}}\right)\frac{\partial {p_f}^n}{\partial t} - \frac{b^2}{K_{dr}}\frac{\partial {p_f}^{n-1}}{\partial t} - \frac{k_f}{\mu_f}(\nabla^2 {p_f}^n) + \lambda_t T_{f-m}(p^n - {p_f}^n) = q. \quad (24)$$

Eq. 24 is added to the system of equations to solve for fracture pressure (p_f); M_f is the Biot modulus inside the fracture domain calculated using modified porosity obtained from Eq. 18; and k_f is fracture permeability.

Numerical Model

As stated previously, OpenFOAM has been used as a main solver for our model. Discretization uses the FVM, which is up to second-order accuracy and consists of time and space. Time discretization is an implicit method with first-order accuracy, whereas spatial discretization consists of both implicit and explicit methods, in which the majority is dependent on the Gaussian linearization method. Discretization, discussed in Tang et al. (2015), can be written in an integral form representing the control volume (∂V) of each cell. Geomechanics (Eq. 14) can be rewritten using Gauss's theorem to convert the volume integral to the surface integral as

$$\oint_{\partial V} \mathrm{d}s \cdot [(2\mu + \lambda)\nabla u] = -\int_{\partial V} \mathrm{d}s \cdot [\mu \nabla u^T + \lambda I tr(\nabla u) - (\mu + \lambda)\nabla u] + \oint_{\partial V} \mathrm{d}s \cdot (bpI) - \oint_{\partial V} \mathrm{d}s \cdot (bp_0 I + \sigma_0). \quad (25)$$

The term on the left-hand side of Eq. 25 is the implicit surface-diffusion term, whereas the terms on the right-hand side are, in order, the explicit surface-diffusion term, the explicit pressure-coupling term, and the explicit constant term representing the initial state. In addition, the fluid flow of Eq. 23 can be rewritten as

$$\int_V \left[\left(\frac{1}{M} + \frac{b^2}{K_{\mathrm{dr}}}\right)\frac{\partial p^n}{\partial t}\right] \mathrm{d}V - \oint_{\partial V} \mathrm{d}s \cdot \left(\frac{k}{\mu}\nabla p^n\right) = \int_V \left(\frac{b^2}{K_{\mathrm{dr}}}\frac{\partial p^{n-1}}{\partial t}\right) \mathrm{d}V - \oint_{\partial V} \mathrm{d}s \cdot \frac{\partial u}{\partial t} - \int_V [\lambda_t T_{f-m}({p_f}^n - p^n)]\, \mathrm{d}V. \quad (26)$$

The first term on the left-hand side of Eq. 26 is an explicit term representing pressure from a previous timestep, the second term is an explicit displacement coupling term, and last term is an explicit source/sink term. The fluid-flow equation inside fractures (Eq. 24) can be discretized in a manner similar to that for Eq. 26:

$$\int_V \left[\left(\frac{1}{M_f}+\frac{b^2}{K_{dr}}\right)\frac{\partial {p_f}^n}{\partial t}\right]\mathrm{d}V - \oint_{\partial V}\mathrm{d}s\cdot\left(\frac{k_f}{\mu}\nabla {p_f}^n\right) = \int_V \left(\frac{b^2}{K_{dr}}\frac{\partial {p_f}^{n-1}}{\partial t}\right)\mathrm{d}V - \int_V [\lambda_t T_{f-m}(p^n - {p_f}^n)]\,\mathrm{d}V + \int_V q\mathrm{d}V. \qquad (27)$$

The traction boundary condition can also be discretized in the manner used for Eq. 25 with implicit and explicit splits, but only at the boundary surfaces. With the discretization, the system of five equations consisting of three displacement equations and fluid-flow equations in matrix and fractures with five unknowns (i.e., u_x, u_y, u_z, p, and p_f) can then be solved sequentially using the iterative method. Effective stress and total stress can be computed after obtaining displacement components and pressure using Eq. 2.

Validation

This section is divided into two subsections. The first part is the coupled fluid-flow/geomechanics model, and the second part is the implementation of EDFM in our coupled model.

Coupled Fluid-Flow/Geomechanics Model. We validated our coupled model with classical poroelasticity problems consisting of the Terzaghi (1925) (1D) **(Fig. 2a)** and Mandel (1953) (2D) (Fig. 2b) problems. We assume that the isothermal porous media is composed of single-phase fluid and solid and behaves as linear poroelastic.

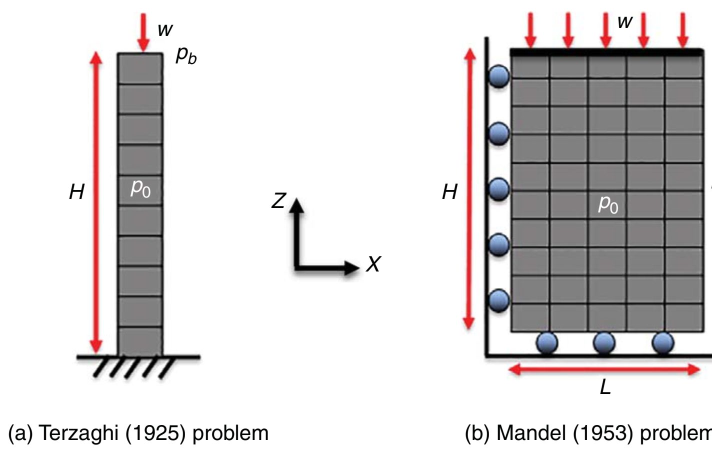

Fig. 2—Diagram for (a) Terzaghi problem and (b) Mandel problem.

Terzaghi Problem. The Terzaghi (1925) problem deals with the 1D consolidation of a fluid-saturated column with a drainage boundary at the top domain and a no-flow boundary at the bottom domain. A constant load (w) is applied instantaneously at time $t = 0$. The problem geometry is shown in Fig. 2a. The column height, $H = 15$ ft, is subdivided into 10 gridblocks of uniform size $z = 1.5$ ft. Gravity effect is neglected for this problem. Poroelastic parameters used for this problem are shown in **Table 1.** Initial pressure (p_0) is 1,450 psi and displacement is zero everywhere. A 2,900-psi load (w) is applied on top of the domain, whereas zero-displacement boundary condition is applied on bottom of the domain. Fluid is only allowed to flow out at the top of the domain with boundary pressure of 1,450 psi, and there is no flow on the bottom of the domain. As shown in **Fig. 3a,** the solution for vertical displacement computed by our model (dots) is compared with the analytical solution (lines) specified in detail in Appendix A.

Parameter	Value	Unit
Young's modulus (E)	1.45×10^5	psi
Poisson's ratio (v)	0	–
Biot coefficient (b)	1	–
Reservoir permeability (k)	50	md
Reservoir porosity (ϕ)	0.25	–
Fluid compressibility (c_f)	2.76×10^{-5}	psi^{-1}
Fluid viscosity (μ_f)	1	cp

Table 1—Parameters used in calculation of the Terzaghi (1925) problem.

Fig. 3b shows a comparison between analytical and numerical solutions for both pressure (p) and vertical displacement (u_z) at various characteristic times: $t_d = \dfrac{kt}{\mu(\phi c_f + \frac{1}{K_{dr}})L^2}$. We obtain a good agreement for both pressure and displacement at early and late times. Initially, pressure along the column increases to approximately 1.5 times the initial pressure and then decreases as the fluid flows out at the bottom of the domain. Linear displacement along the z-direction increases with time because there is less pressure to support the column.

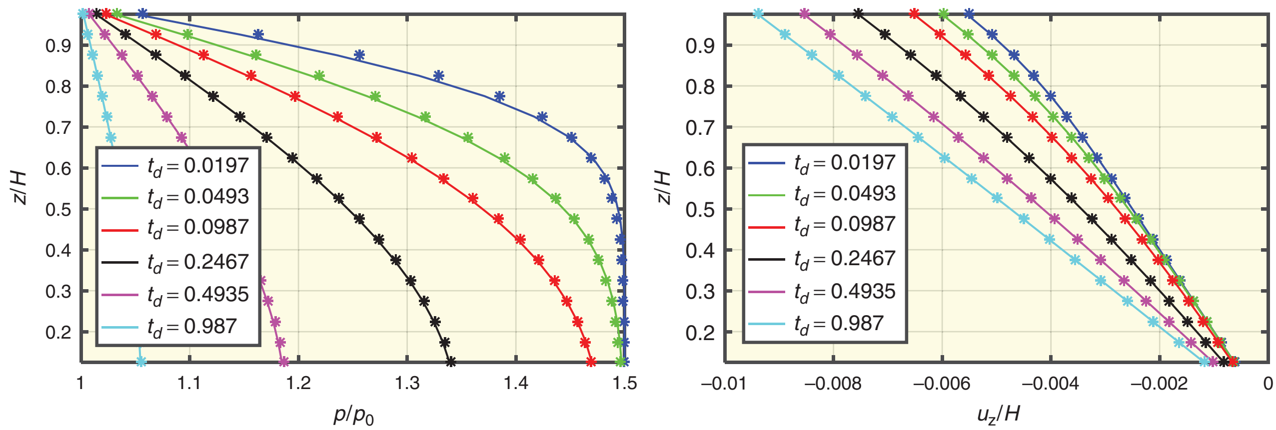

(a) Pressure plot at various times

(b) Displacement in x-direction plot at various times

Fig. 3—Comparison of numerical solution (dots) for (a) pressure, (b) horizontal displacement with the analytical solution (lines) along the *x*-direction at various characteristic times.

Mandel Problem. The Mandel problem deals with 2D consolidation of a fluid-saturated slab sandwiched between two rigid, frictionless, and impermeable plates with compressive force being applied on both sides (Mandel 1953). A traction-free boundary is applied on both the left and right boundaries, with fluid being allowed to flow out. A main feature of this classical problem is the Mandel-Cryer effect (Cryer 1963), which is the instant increase of pressure at the middle of the slab because of two-way coupling between fluid flow and solid deformation. To achieve this, uniform vertical displacement (in the z-direction) along the x-direction must be maintained at all times. This can be done by modeling the stiff plate (impervious material) on top of porous material (Lee 2008) or using time-dependent displacement boundary condition calculated from analytical solution (Wang 2014). In this case, rather than modeling a stiff plate, we used the geometry in Fig. 2b (length in y-direction is longer than x-direction, like a column) to ensure uniform vertical displacement. Because of the symmetry of this problem, the simulation was run only for one-quarter of the domain by assigning the left and bottom boundaries as no flow for the fluid part, and the roller boundary as shown in Fig. 2b (zero normal displacement) for the geomechanics part. The domain is 30 ft long (x-direction) and 300 ft high (z-direction) with 20 gridblocks along the x-direction and 200 gridblocks along the z-direction. Details of the parameters used in this problem are shown in **Table 2.** Initial pressure (p_0) is 0 psi, including the pressure at boundary (p_b), and displacement in both the x- and z-direction are zero everywhere. A 616-psi load (w) is uniformly applied on top of the domain, zero displacement in normal direction is used for the left and bottom of the domain to represent symmetry boundary, and the right boundary of the domain is traction-free. Fluid is only allowed to flow out on the right boundary, with boundary pressure being set as 0 psi and other boundaries being no-flow. Solutions for pressure, x-displacement along the x-direction, and the vertical stress along the z-direction computed by our model (dots) are compared with the analytical solution (lines). The analytical solution is provided in detail in Appendix A.

Parameter	Value	Unit
Young's modulus (E)	6.52×10^{4}	psi
Poisson's ratio (v)	0	–
Biot coefficient (b)	1	–
Reservoir permeability (k)	50	md
Reservoir porosity (ϕ)	0.25	–
Fluid compressibility (c_f)	2.76×10^{-6}	psi^{-1}
Fluid viscosity (μ_f)	1	cp

Table 2—Parameters used in calculation of the Mandel (1953) problem.

Fig. 4 shows a comparison between analytical (lines) and numerical solutions (dots) for pressure (p), vertical stress (σ_{yy}), and horizontal displacement (u_x) at various characteristic times (t_d). Our model produces similar solutions compared with the analytical solution at both early and late times. Initially, a uniform pressure, 313 psi, which is approximately one-half of the load being applied on the top boundary, is generated because of the Skempton effect (Skempton 1954). The Mandel-Cryer effect can then be observed at $t_d = 0.085$, illustrating a rise in pressure of approximately 10%. After this point, pressure starts to decrease because of the flow boundary until it reaches an initial value, which is $p = 0$ psi at late time. The vertical stress (y-direction) increases more than the external load (w) at the center because of the Mandel-Cryer effect. As pressure starts to decrease, σ_{yy} approaches a uniform value, which is the value of external load (w). The largest horizontal displacement (u_x) can be observed at the right boundary because the plate is fixed at the center. u_x for the entire domain decreases to zero with time because of the fluid flowing out from the domain.

The Coupled Model With EDFM. Our coupled geomechanics/fluid flow with EDFM using uniform structure grids is validated against local grid refinement for a 0°-angle-of-inclination fracture and against a refined grid for a 45°-angle-of-inclination fracture on a

2D reservoir. **Fig. 5** shows fracture geometry on local grid refinement and refined grid (zoomed-in area around fracture) with $L_x = 2{,}420$ ft and $L_y = 1{,}820$ ft with $N_x = 121$, $N_y = 95$ for a 0°-angle-of-inclination fracture, and $N_x = 347$, $N_y = 317$ for a 45°-angle-of-inclination fracture. For the EDFM case, we used a uniform grid with $N_x = 121$, $N_y = 91$ for both 0 and 45° angles of inclination. Parameters used in simulation are shown in **Table 3.** The fracture is along the x-direction. Initially, the stress in the x-direction is 4,600 psi and the stress in the y-direction is 4,500 psi. The initial reservoir pressure is 4,000 psi.

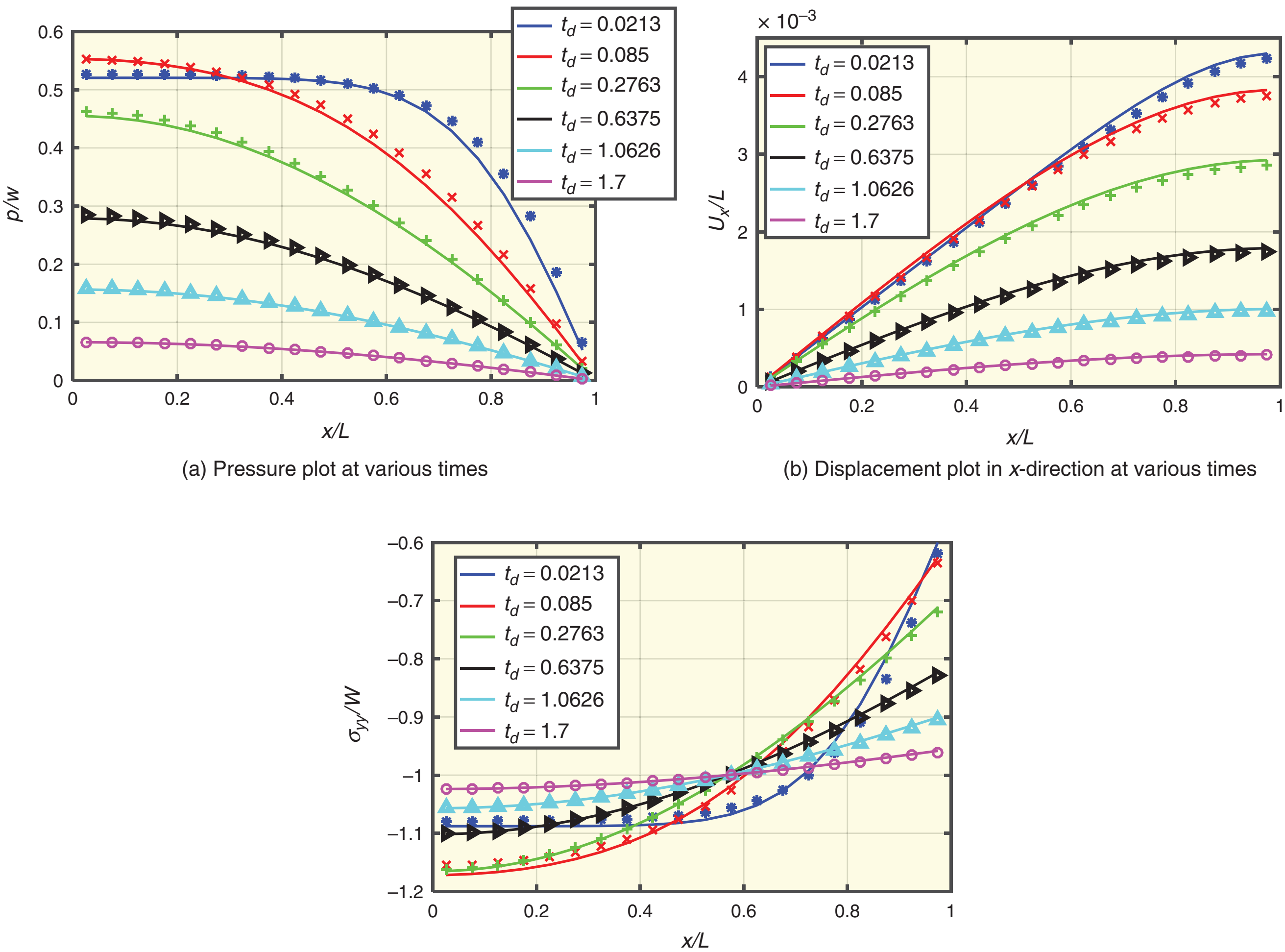

(a) Pressure plot at various times

(b) Displacement plot in x-direction at various times

(c) Stress in y-direction plot at various times

Fig. 4—Comparison of numerical solution (dots) for (a) pressure and (b) displacement with analytical solution (lines) along the *z*-direction at different characteristic times. (a) Pressure plot at various times; (b) displacement plot in *x*-direction at various times; (c) stress in *y*-direction plot at various times.

Figs. 6 and 7 provide a comparison between local grid refinement and our model for reservoir pressure (p) (Figs. 6a, 6b, 7a, and 7b), σ_{xx} (Figs. 6c, 6d, 7c, and 7d), and σ_{yy} (Figs. 6e, 6f, 7e, and 7f) distribution for 0 and 45° cases. σ_{yy} and σ_{xx} are the current reservoir stresses after depletion. As shown in Figs. 6 and 7, the difference between our model and local grid refinement is insignificant for both 0 and 45° cases. Pressure is observed being depleted in an elliptical shape because of its geometry. σ_{xx} increases on the top and bottom parts of the domain to support pressure depletion in the x-direction, whereas σ_{yy} increases on the right and left parts of the domain to support pressure depletion in the y-direction. Flow rate for all four cases is calculated using the Peaceman (1993) equation with 0.25-ft well radius. Comparison in **Fig. 8** yields good matching among all cases with 0° having slightly higher flow rate because of the larger depletion area. This implies that the angle of inclination plays an important role in well performance. In addition, our model provides a significant improvement in computational efficiency. Although this cannot be observed in the 0° case because the number of cells is very similar for our model and local refinement, the 45° case reduces the computational time from 4 hours of local refinement to the 0.5 hours of our model. This is important for future studies that consider complex-fracture geometry.

Case Studies

In this section, we focus on studying the effects of fracture geometry on stress distribution and reorientation in the field. The boundary condition needs to be appropriately chosen to accurately simulate actual conditions in the field. In the following subsections, the effects of boundary conditions were investigated to illustrate the role that boundary conditions play in the flow/stress calculation.

Effect of Boundary Condition. In this subsection, we compare pressure and stress distribution between constrained and unconstrained boundary conditions. Similar comparison was conducted by Dean et al. (2006), with the focus on reservoir pressure and surface subsidence compared between constrained and unconstrained boundary conditions. Reservoir and fracture geometry are shown in **Fig. 9.**

Table 4 provides the parameters used in the simulation. This set of parameters is derived from the Bakken Reservoir, which was given in Roussel et al. (2013). The domain has length of 755 ft (L_x), width of 755 ft (L_y), and height of 100 ft (L_z). The domain was discretized to 151 cells in the x- and y-direction and one cell in the z-direction. The constrained boundary condition has 11,000 psi applied on the boundary in the x-direction, 11,500 psi applied on the boundary in the y-direction, 13,000 psi applied on the top boundary in the z-direction, and zero displacement on the bottom boundary. The unconstrained boundary condition has zero displacements on all boundaries, except the top boundary in the z-direction, with 13,000-psi traction stress. A no-flow boundary is applied on all six boundaries to contain fluid from flowing out, thus pressure in the reservoir can only decrease because of production.

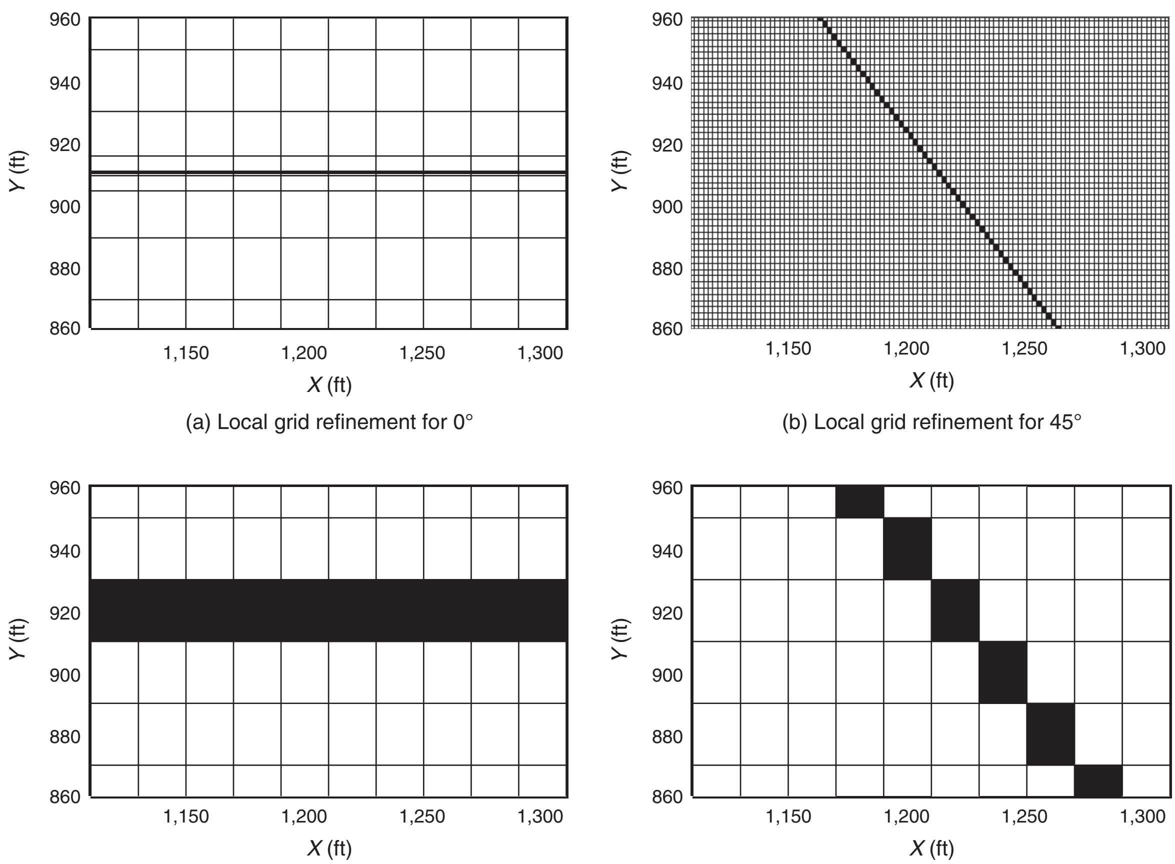

Fig. 5—Grid structure (zoomed-in area around fractures) for (a) 0° grid refinement, (b) 45° grid refinement, (c) 0° EDFM, and (d) 45° EDFM angle of inclination.

Parameter	Value	Unit
Young's modulus (E)	1×10^6	psi
Poisson's ratio (v)	0.3	–
Biot coefficient (b)	0.7	–
Reservoir permeability (k)	10	md
Reservoir porosity (ϕ)	0.05	–
Fluid compressibility (c_f)	2×10^{-4}	psi^{-1}
Fluid viscosity (μ_f)	0.6	cp

Table 3—Parameters used in calculation for a single-fracture-test problem.

Fig. 10 illustrates the comparison of pressure with direction of maximum horizontal stress ($\sigma_{H\max}$), σ_{xx}, and σ_{yy} distributions between constrained and unconstrained boundary conditions at 5 years of production. White dashed lines on top of the pressure distribution in Figs. 10a and 10b represent the orientation of $\sigma_{H\max}$. The difference of pressure distribution is insignificant. However, contour plots of σ_{xx} and σ_{yy} show a significant difference between the two conditions. There is a stress difference of approximately 1,000 psi in the region near the boundaries. The constrained boundary condition allows stress to change at all boundaries, whereas the unconstrained boundary condition enforces stress at the boundaries to remain constant. Therefore, when pressure decreases, stress at the boundaries increases to support boundary force from the unconstrained boundary condition. Distribution at the fracture area is shown to be not very different between constrained and unconstrained boundary conditions, which results in small difference of stress reorientation

(Figs. 10a and 10b). Flow rate and average reservoir pressure remain the same for both cases (**Fig. 11**). From the analysis, we can find that boundary conditions primarily have great effects on stresses near the boundary and nearly no influence on stresses within the drainage area. Because we only focus on a group of four fractures from a well with a multistage-fracturing treatment, the constrained boundary condition is a better choice in this case because it allows stress at all boundaries to change over time. Constraining displacements in the normal direction are a result of production from adjacent fractures or wells. If we were to run the entire reservoir that covers multiple perforations as well as a large area of reservoir, the unconstrained boundary might be a better option because stress at all boundaries is expected to remain constant.

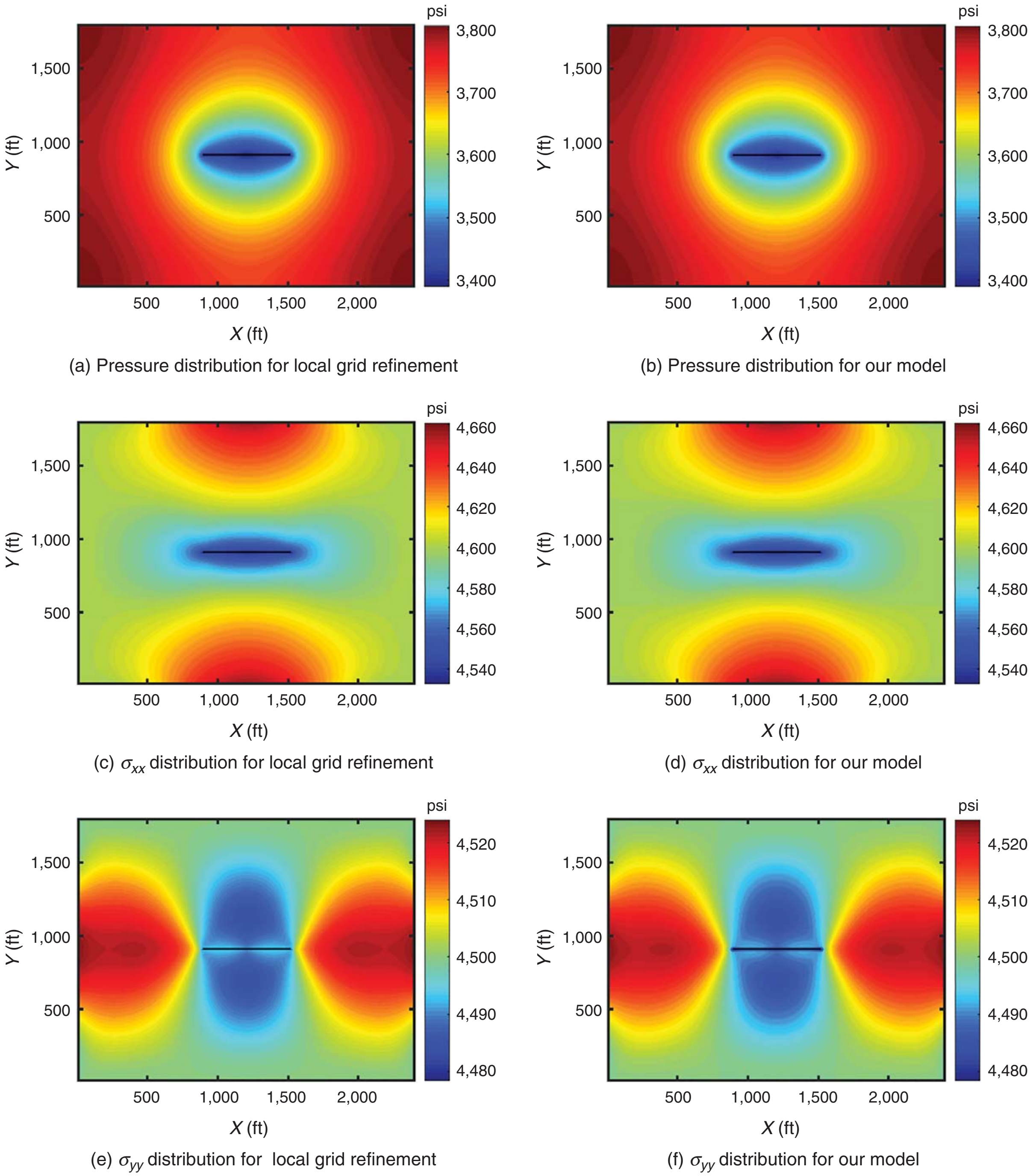

Fig. 6—Comparison between our model (right) and local grid refinement (left) of (a, b) 0° angle of inclination for pressure distribution, (c, d) σ_{xx} distribution, and (e, f) σ_{yy} distribution at 100 days of production.

Effect of Fracture Geometry. In this subsection, we studied how fracture geometries affect stress distribution and reorientation as well as production rate using the constrained boundary condition as discussed previously. With implementation of EDFM in our coupled geomechanics/fluid-flow model, the code is capable of simulating stress change caused by depletion in the reservoir with complex-fracture geometry. Fracture geometries in this study consist of planar-fracture (90° angle of inclination), 60°-inclination, and nonplanar-fracture geometries. We chose fractures with 60° misaligned angle because in some situations horizontal wells are not drilled along the direction of the least principal stress. When fracture interaction has great effects on multiple-fracture propagation, nonplanar-fracture geometry can be generated in the field. The nonplanar-fracture geometry was obtained using our in-house fracture-propagation model, which predicts fracture propagation incorporating stress-shadowing effects. To make comparisons, all three geometries have been created with the same surface area. The same set of parameters and reservoir size found in the preceding subsection are used here to represent simulation in the Bakken Reservoir. **Figs. 12 and 13** show pressure distribution with direction of $\sigma_{H\max}$ and $\sigma_{yy} - \sigma_{xx}$ of the three fracture geometries at 1 and 5 years of production.

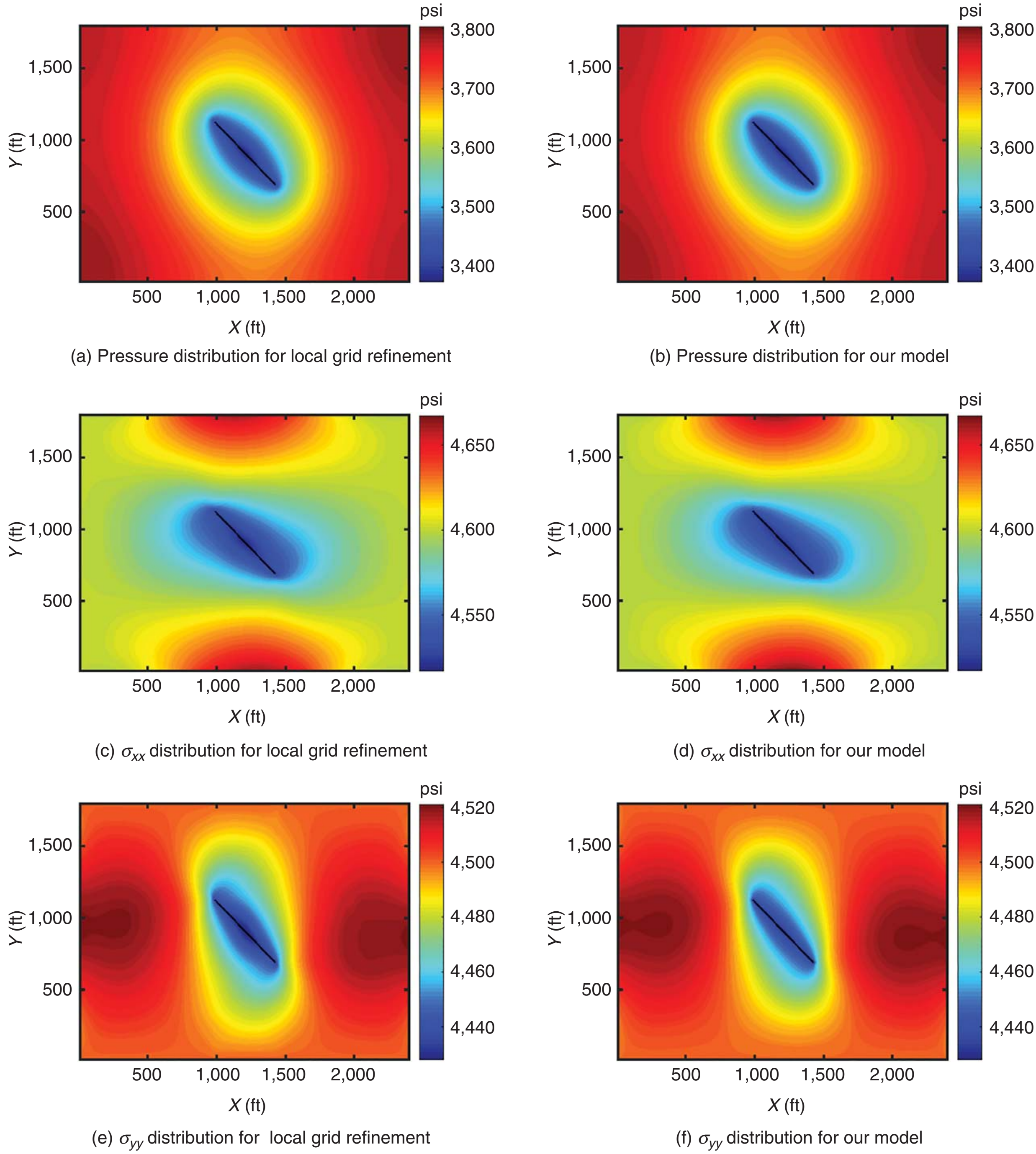

Fig. 7—Comparison between our model (right) and local grid refinement (left) of (a, b) 45° angle of inclination for pressure distribution, (c, d)σ_{xx} distribution, and (e, f) σ_{yy} distribution at 100 days of production.

As shown in Fig. 12, all three cases have different drainage areas. Nonplanar-fracture geometry has the largest depleted area, followed by 60°-inclination and planar-fracture geometries. This directly affects production rate, which corresponds to the size of the depleted area, as shown in Fig. 13. Nonplanar-fracture geometry has the largest area resulting in highest production, followed by planar-fracture geometries and 60° inclination, respectively. There is nearly no difference in production between the planar fracture and 60°-inclination geometry, which is a result of similar drainage size. Another observation from these plots is the direction of maximum horizontal stress, which originally is in the y-direction (fracture-propagation direction). After 1 year of production, we start to see some angle changes around fracture tips for all three cases. In addition, after 5 years of production, more angle changes, especially at the depleted area, can be observed. Stress reversal (stress rotates 90° from its original orientation) can mainly be observed at the inner fractures around the depleted area only for planar-fracture geometry. Similarly, stress rotates 60° from its original orientation for 60° inclination fracture geometry, becoming perpendicular to fracture orientation. This is because of the shape of the depleted area, which will be further discussed in the next subsection.

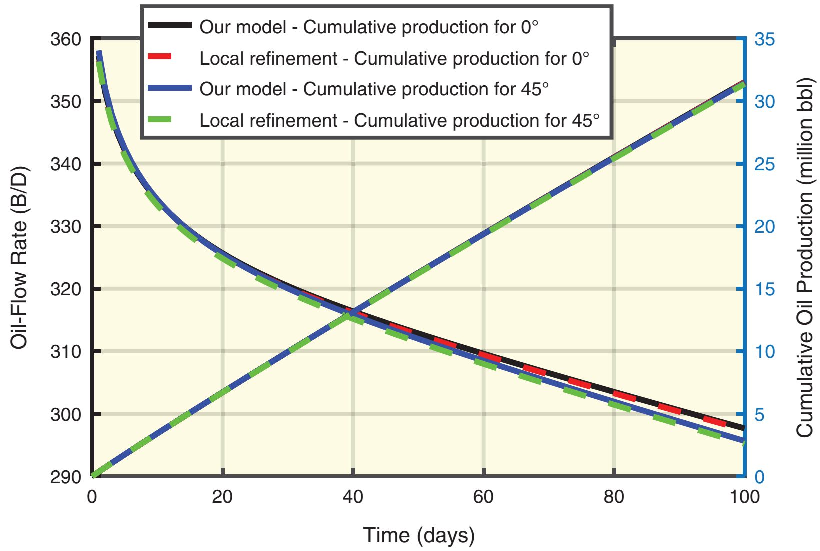

Fig. 8—Flow-rate comparison between our model and local grid refinement for 0 and 45° angles of inclination for 100 days of production.

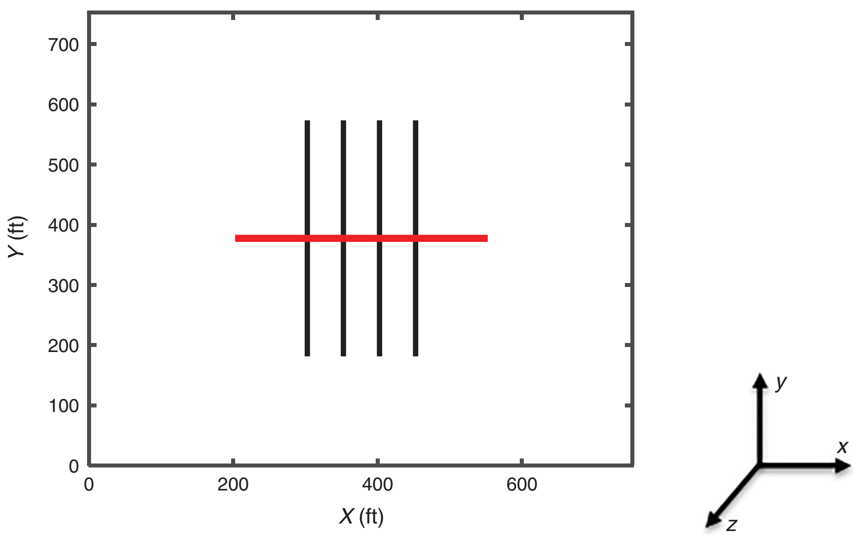

Fig. 9—Reservoir geometry with four planar fractures.

Parameter	Value	Unit
Young's modulus (E)	2×10^6	psi
Poisson's ratio (v)	0.2	–
Biot coefficient (b)	0.7	–
Reservoir permeability (k)	0.304	μd
Reservoir porosity (ϕ)	0.05	–
Fluid compressibility (c_f)	2.18×10^{-5}	psi^{-1}
Wellbore radius (r_w)	0.25	ft
Fluid viscosity (μ_f)	0.25	cp
Initial pressure (p_0)	1×10^4	psi
Initial stress in x-direction ($\sigma_{xx,0}$)	1.1×10^4	psi
Initial stress in y-direction ($\sigma_{yy,0}$)	1.15×10^4	psi
Initial stress in z-direction ($\sigma_{zz,0}$)	1.3×10^4	psi
Fracture spacing	50	ft

Table 4—Parameters used for testing different boundary conditions on multifracture-test problem and case studies for different fracture geometries.

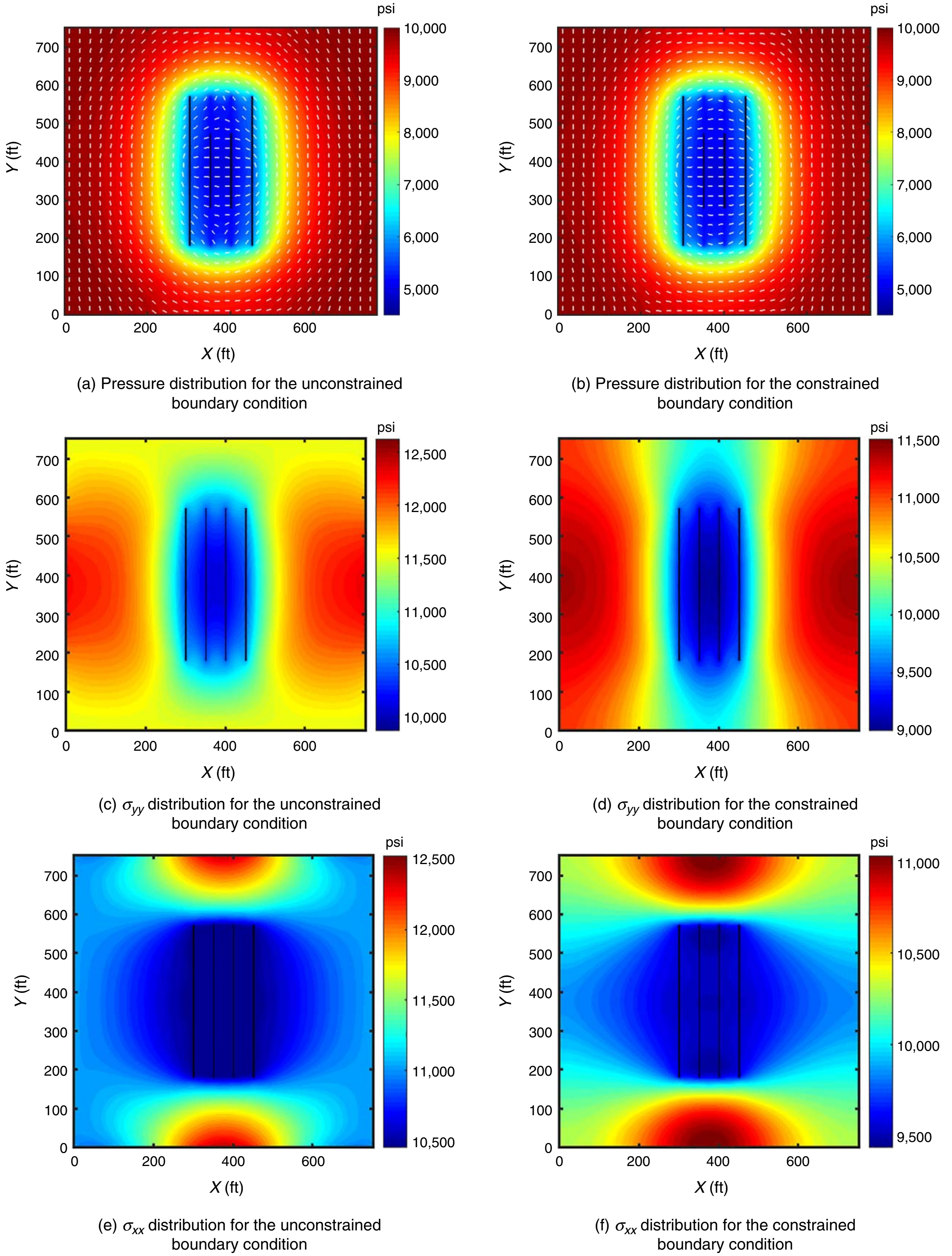

(a) Pressure distribution for the unconstrained boundary condition

(b) Pressure distribution for the constrained boundary condition

(c) σ_{yy} distribution for the unconstrained boundary condition

(d) σ_{yy} distribution for the constrained boundary condition

(e) σ_{xx} distribution for the unconstrained boundary condition

(f) σ_{xx} distribution for the constrained boundary condition

Fig. 10—Comparison between constrained (right) and unconstrained (left) for (top) pressure distribution, (middle) σ_{yy} distribution, and (bottom) σ_{xx} distribution at 5 years of production. (a) Pressure distribution for the unconstrained boundary condition; (b) pressure distribution for the constrained boundary condition; (c) σ_{yy} distribution for the unconstrained boundary condition; (d) σ_{yy} distribution for the constrained boundary condition; (e) σ_{xx} distribution for the unconstrained boundary condition; (f) σ_{xx} distribution for the constrained boundary condition.

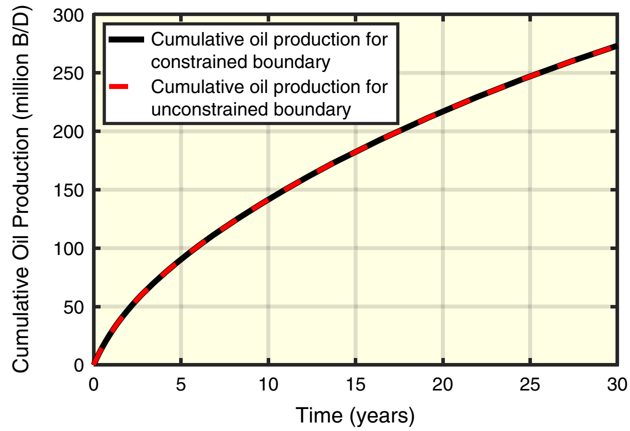

Fig. 11—Flow-rate comparison between constrained and unconstrained boundary conditions.

Furthermore, stress reversal can be observed at the top and bottom area of the fractures for all three cases after 5 years of production. This is because of the reduction in stress difference ($\sigma_{yy} - \sigma_{xx}$), as shown in **Fig. 14,** which represents distribution of stress difference at 1-year and 5-year production times. Originally, σ_{yy} is 500 psi larger than σ_{xx}. After depletion, σ_{yy} decreases more in the top and bottom areas, whereas σ_{xx} in these areas stays nearly the same. Consequentially, the difference between σ_{yy} and σ_{xx} becomes less than its original value. In some areas, σ_{yy} can become smaller than σ_{xx}. In contrast, σ_{xx} decreases more at the right and left boundaries, whereas σ_{yy} remains the same. Thus, in this location, the difference between σ_{yy} and σ_{xx} become larger than its original difference. In the drainage area near fractures, the three different fracture geometries generate significant difference of $\sigma_{yy} - \sigma_{xx}$ distribution. Both σ_{xx} and σ_{yy} decrease with reservoir pressure. σ_{yy} reduces faster than σ_{xx} as a function of depletion. However, decrease rate of σ_{xx} and σ_{yy} is distinct for different fracture geometries. Decrease-rate difference of σ_{xx} and σ_{yy} is much larger for planar-fracture geometry than nonplanar-fracture geometry. Updated stress difference ($\sigma_{yy} - \sigma_{xx}$) of nonplanar-fracture geometry is greater than that of planar-fracture geometry, which implies that the difference of decrease rate of σ_{xx} and σ_{yy} is smaller for nonplanar-fracture geometry. In most regions within the drainage area, the stress difference is still larger than zero for nonplanar-fracture geometry, whereas the difference is less than zero for planar-fracture geometry. Once σ_{yy} becomes smaller than σ_{xx}, stress reversal will occur.

Effect of DS ($\boldsymbol{\sigma_{xx,0} - \sigma_{yy,0}}$). DS is defined as the difference between the two horizontal principal stresses in the reservoir before depletion. Because two principal stresses are initially in the x- and y-direction, DS is the difference between $\sigma_{xx,0}$ and $\sigma_{yy,0}$. DS plays an important role in stress reorientation because the smaller it is, the higher chance that reorientation will occur. In this section, DS is 500 psi, which is a base case in the preceding subsection, as well as 250 and 100 psi. To study how new fractures would propagate during refracturing or completion of infill wells when existing fractures are under production, it is important to be able to predict stress reorientation, which defines the direction of new fracture propagation. $\sigma_{xx,0}$ and $\sigma_{yy,0}$ are the initial reservoir stresses before depletion, whereas σ_{yy} and σ_{xx} are current reservoir stresses after depletion. $\Delta\sigma_{yy}$, $\Delta\sigma_{xx}$, and $\Delta\sigma_{xy}$ are stress changes induced by depletion. The relationship between stresses can be expressed as

$$\begin{aligned}
&\sigma_{yy} - \sigma_{xx} = \sigma_{yy,0} + \Delta\sigma_{yy} - \sigma_{xx,0} - \Delta\sigma_{xx},\\
&\sigma_{yy} - \sigma_{xx} = (\sigma_{yy,0} - \sigma_{xx,0}) + \Delta\sigma_{xx} - \Delta\sigma_{yy},\\
&\sigma_{yy} - \sigma_{xx} = DS + \Delta\sigma_{xx} - \Delta\sigma_{yy}, \qquad (28)
\end{aligned}$$

Fig. 15 illustrates the induced stress difference ($\Delta\sigma_{yy} - \Delta\sigma_{xx}$) plotted along the x-direction at $y = 377.5$ ft for all three geometry cases at 1, 5, and 30 years. According to Eq. 28, this plot can be applied for any initial DS because it is written in terms of DS, which is a constant value. $\sigma_{yy} - \sigma_{xx}$ is an updated stress difference after production and only changes when DS changes for a specific $\Delta\sigma_{yy} - \Delta\sigma_{xx}$. If the initial DS is 0 psi, any areas of the plot that are less than 0 psi represent stress reversal. The same mechanism applies for other different stresses; [i.e., 100 psi (pink line) and 500 psi (green line) in Fig. 15].

A very small magnitude of induced shear stress ($\Delta\sigma_{xy}$) is observed on planar- and nonplanar-fracture geometries (Figs. 15b and 15f). The inclination fracture geometry produces a large shear stress as a result of inclination of fractures causing stress to rotate to 60°. Because the magnitude of induced shear stress is small compared with induced horizontal stresses, a main factor that causes stress to reorient is the difference between $\Delta\sigma_{xx}$ and $\Delta\sigma_{yy}$. Therefore, we focus on the induced stress difference $\Delta\sigma_{yy} - \Delta\sigma_{xx}$ because it directly affects the calculation of reorientation.

For planar-fracture geometry (Fig. 15a), stress reorientation between inner fractures can be observed from DS = 0 psi up to approximately 500 psi at 1 year and 850 psi at 5 years. We can also observe stress reorienting back after 30 years of production. This result corresponds to the preceding subsection, in which stress reorientation at the depleted area can be observed the most in planar-fracture geometry. The angle change of maximum horizontal stress ($\sigma_{H\max}$) can be found in **Fig. 16** for DS = 100 and 500 psi. This aligns with plots of $\Delta\sigma_{yy} - \Delta\sigma_{xx}$ because both cases reorient 90° at the depleted area between two inner fractures.

On the other hand, for 60°-inclination fracture geometry (Fig. 15c), no reorientation can be observed for DS = 400 psi or more. This implies that if the original DS is 500 psi, which is our base case, there will be no stress reorientation. After 30 years of production, stress starts to reorient back just like planar-fracture geometry. Fig. 16 shows orientation change at DS = 100 and 500 psi, which confirms that only a small orientation change occurs at DS = 500 psi (Figs. 16a, 16c, and 16e) for planar-fracture geometry and 60°-inclination fracture geometries. No change can be observed for nonplanar-fracture geometry. A larger orientation change occurs at DS = 100 psi for all three geometries, especially in the region between inner fractures (Figs. 16b, 16d, and 16f). Maximum angle change for 60°-inclination fracture geometry is only 53°, which is very close to the initial fracture direction (60°), but in the perpendicular direction. Meanwhile, the maximum angle change for the other two cases is 90° or fully reversed.

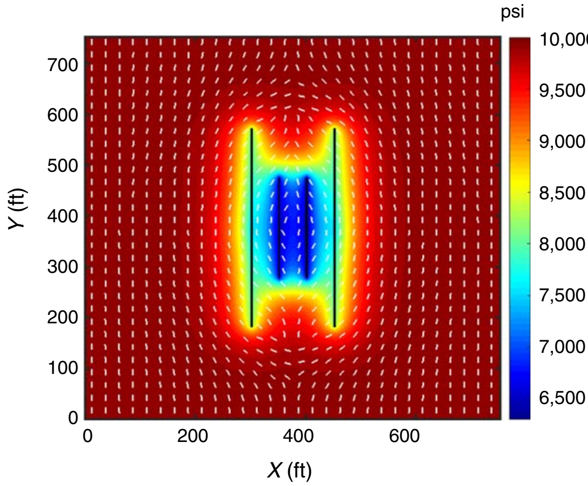

(a) Pressure distribution for planar-fracture geometry with direction of maximum horizontal stress at 1 year

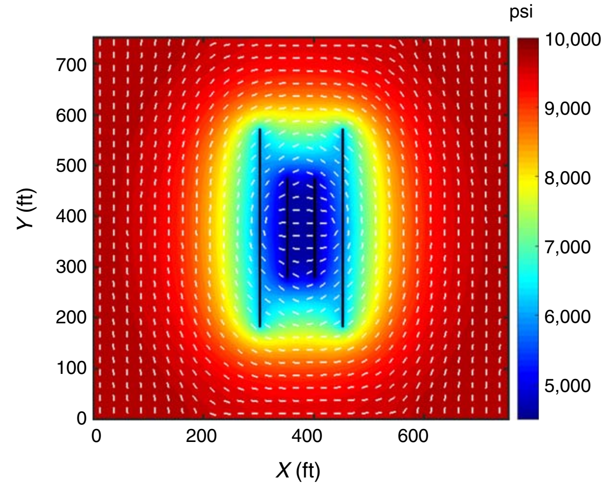

(b) Pressure distribution for planar-fracture geometry with direction of maximum horizontal stress at 5 years

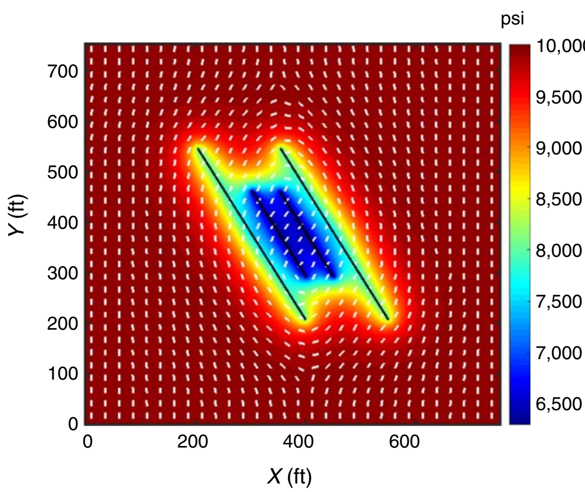

(c) Pressure distribution for 60° fracture geometry with direction of maximum horizontal stress at 1 year

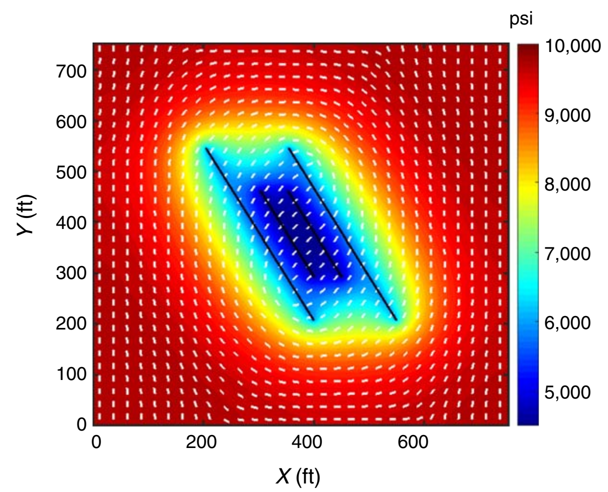

(d) Pressure distribution for 60° fracture geometry with direction of maximum horizontal stress at 5 years

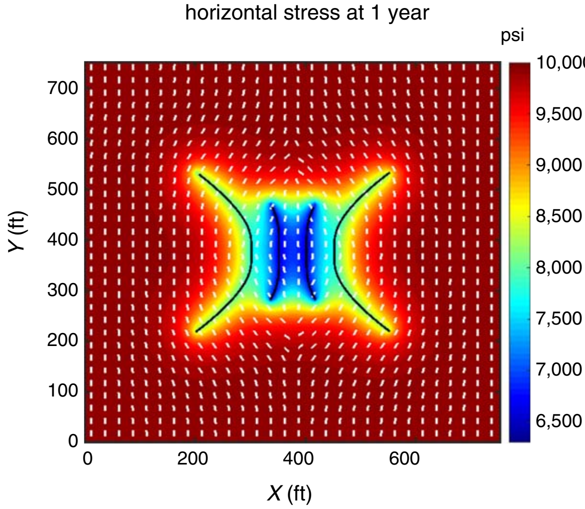

(e) Pressure distribution for nonplanar-fracture geometry with direction of maximum horizontal stress at 1 year

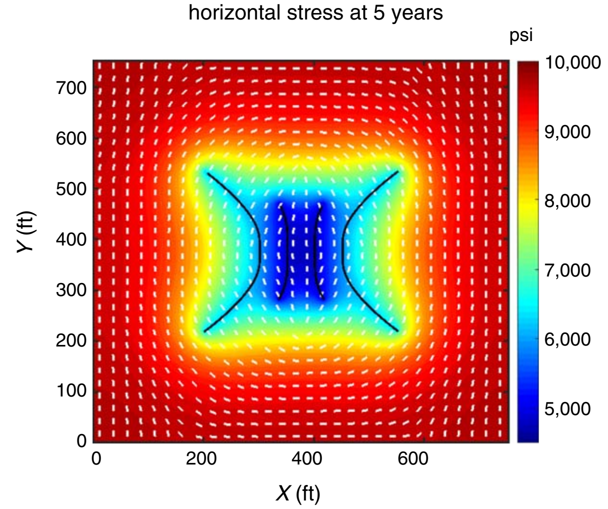

(f) Pressure distribution for nonplanar-fracture geometry with direction of maximum horizontal stress at 1 year

Fig. 12—(a, b) Pressure distribution with direction of maximum horizontal stress of planar-fracture geometry; (c, d) 60°-inclination fracture geometry; and (e, f) nonplanar-fracture geometry at 1 and 5 years. (a) Pressure distribution for planar-fracture geometry with direction of maximum horizontal stress at 1 year; (b) pressure distribution for planar-fracture geometry with direction of maximum horizontal stress at 5 years; (c) pressure distribution for 60° fracture geometry with direction of maximum horizontal stress at 1 year; (d) pressure distribution for 60° fracture geometry with direction of maximum horizontal stress at 5 years; (e) pressure distribution for nonplanar-fracture geometry with direction of maximum horizontal stress at 1 year; (f) pressure distribution for nonplanar-fracture geometry with direction of maximum horizontal stress at 1 year.

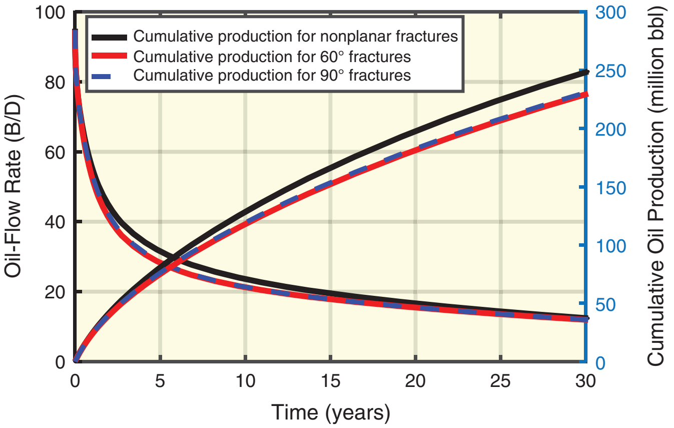

Fig. 13—Flow-rate and cumulative production comparison between planar-fracture, 60°-inclination fracture, and nonplanar-fracture geometries.

Similarly, no stress reorientation is observed on nonplanar-fracture geometry (Fig. 15e) for any DS greater than 250 psi. At DS = 100 psi, some reorientation can be observed, but the area is small compared with planar-fracture geometry and 60°-inclination fracture geometry. It can be seen from Fig. 15 that there is no reorientation for DS = 500 psi even after 30 years of production. However, for DS = 100 psi, reorientation can be observed between inner fractures from 1 to 30 years of production. This corresponds to Fig. 15e, where $\Delta\sigma_{yy} - \Delta\sigma_{xx}$ is less than zero between inner fractures.

As mentioned in the preceding subsection, stress reorientation occurs when σ_{yy} becomes smaller than σ_{xx}. This phenomenon can be observed in the depleted area that has different depletion rates in the x- and y-direction (rectangular shape). Large reduction in the y-direction causes σ_{yy} to decrease faster than σ_{xx} and finally become less than σ_{xx}, creating stress reorientation. Depletion in rectangular shape can be observed in planar-fracture geometry and 60° inclination-fracture geometry. The squared shape of the drainage area can be observed in nonplanar-fracture geometry, which results in small difference of stress change in the x- and y-direction and small likelihood of stress reorientation. It is noted that stress can rotate back if σ_{yy} again becomes larger than σ_{xx}. It is possible to observe this phenomenon around the fracture area, especially between inner fractures. This is because both σ_{xx} and σ_{yy} decrease at different rates at different production periods.

Conclusions

A geomechanics/fluid-flow finite-volume-based model has been successfully developed using the fixed-stress method to ensure stability for high-coupling-strength problems and has been coupled with EDFM to simulate the poroelastic effect of complex-fracture geometry in unconventional reservoirs. This opens the possibility of simulating multiple hydraulic fractures in reservoirs with highly complex-fracture geometries to study stress evolution during depletion. The model was validated against classical poroelastic problems as well as local grid refinement to ensure accuracy for coupled geomechanics/fluid flow with EDFM. The constrained boundary condition was chosen to represent the actual condition in the field. The simulations were run for three different types of geometries using parameters from the Bakken Reservoir. Different fracture geometries result in different shapes of depleted area as well as stress redistribution and reorientation. Decrease rates of two horizontal principal stresses are distinct for different fracture geometries. Rectangular shape with longer drainage dimension in the y-direction can be found in planar-fracture geometry. Squared shape with similar drainage dimension in both the x- and y-direction can be found in nonplanar-fracture geometry. The shape of the depleted area has a significant effect on stress changes in the x- and y-direction and stress reorientation. The rectangular shape yields the largest stress reorientation, whereas the squared shape has much smaller likelihood to create stress reorientation. Large induced shear stress can be observed in inclined-fracture geometries. Reorientation observed from these cases tends to be the same angle as created fractures. In addition, DS also plays an important role in stress reorientation. The smaller the DS, the higher chance of the stress to reorient. The results simulated by our model indicate that it is important to simulate fracture geometry as close to what actually exists in the reservoir to accurately predict stress redistribution and reorientation rather than simulating planar-fracture geometry, which can easily be simulated using a typical coupled geomechanics/fluid-flow simulator. It is crucial for applications of refracturing and completion of infill wells to understand how stress in the reservoir changes after a period of production time. These findings can provide not only a fundamental guideline for selecting the best candidates to perform refracturing and for optimizing fracturing design of infill wells, but also a tool to predict the direction of new fracture propagation.

Nomenclature

A_f = area of fracture segment, ft^2
b = Biot coefficient, dimensionless
c_f = fluid compressibility, psi^{-1}
C_{dr} = Rank 4 elastic tensor, psi
d_{f-m} = average normal distance from matrix to fracture, ft
d_{f1} = weighted average of the normal distances from centroids of subsection to the intersection line in Cell 1, ft
d_{f2} = weighted average of the normal distances from centroids of subsection to the intersection line in Cell 2, ft
E = Young's modulus, psi
g = gravitational acceleration, ft · s^{-2}
H = domain height, ft
k = matrix permeability, md
k_f = permeability inside fracture domain, md
k_{f1} = permeability inside Fracture Cell 1, md

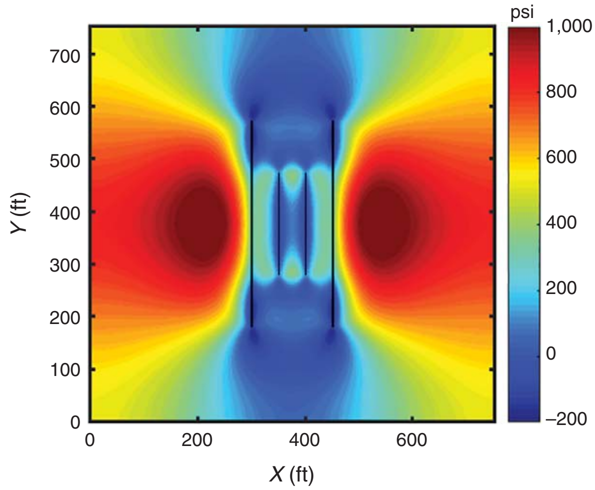

(a) $\sigma_{yy} - \sigma_{xx}$ distribution for planar-fracture geometry at 1 year

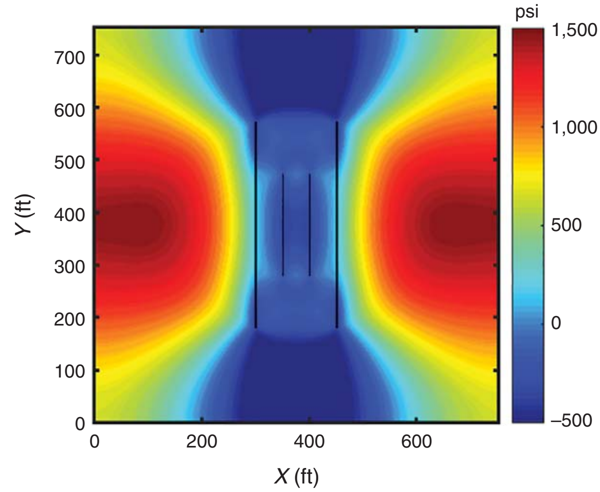

(b) $\sigma_{yy} - \sigma_{xx}$ distribution for planar-fracture geometry at 5 years

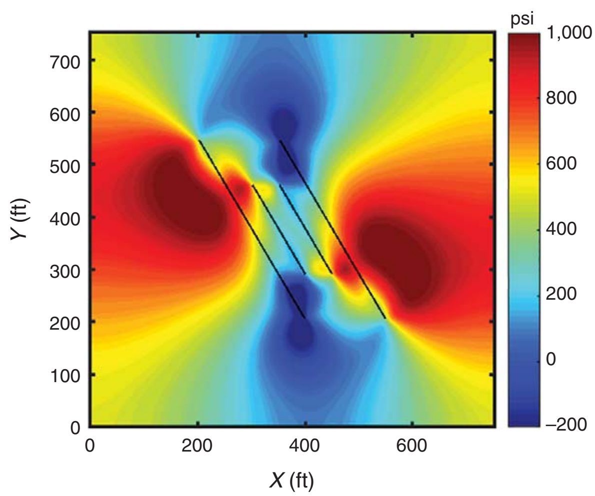

(c) $\sigma_{yy} - \sigma_{xx}$ distribution for planar-fracture geometry at 1 year

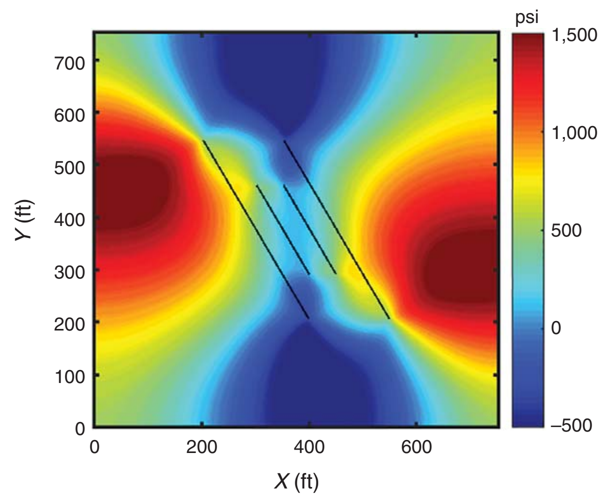

(d) $\sigma_{yy} - \sigma_{xx}$ distribution for planar-fracture geometry at 5 years

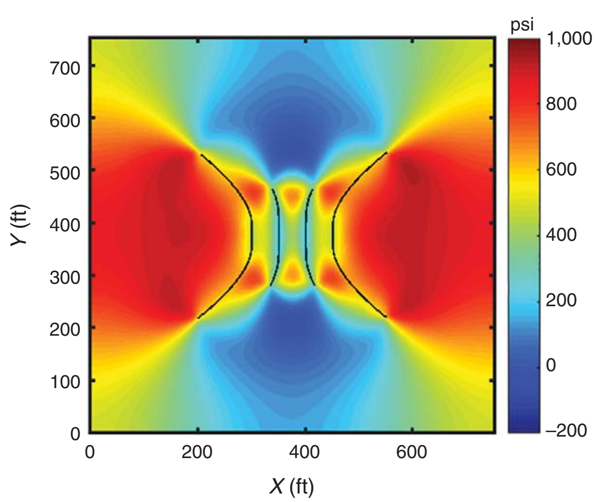

(e) $\sigma_{yy} - \sigma_{xx}$ distribution for planar-fracture geometry at 1 year

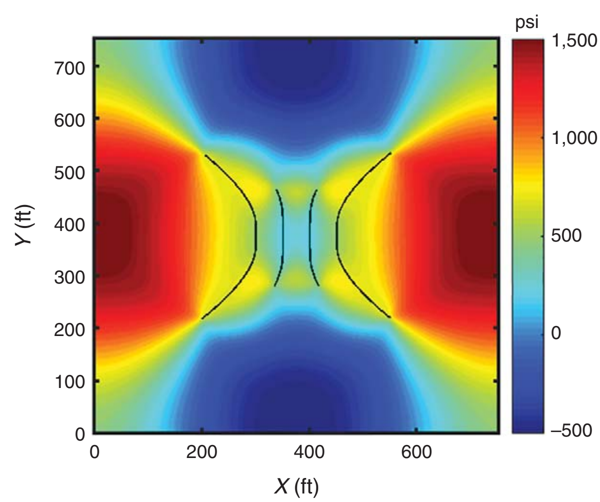

(f) $\sigma_{yy} - \sigma_{xx}$ distribution for planar-fracture geometry at 5 years

Fig. 14—(a, b)$\sigma_{yy}-\sigma_{xx}$ distribution of planar-fracture geometry; (c, d) 60°-inclination fracture geometry; and (e, f) nonplanar-fracture geometry at 1 and 5 years. (a) $\sigma_{yy}-\sigma_{xx}$ distribution for planar-fracture geometry at 1 year; (b) $\sigma_{yy}-\sigma_{xx}$ distribution for planar-fracture geometry at 5 years; (c) $\sigma_{yy}-\sigma_{xx}$ distribution for planar-fracture geometry at 1 year; (d) $\sigma_{yy}-\sigma_{xx}$ distribution for planar-fracture geometry at 5 years; (e) $\sigma_{yy}-\sigma_{xx}$ distribution for planar-fracture geometry at 1 year; (f) $\sigma_{yy}-\sigma_{xx}$ distribution for planar-fracture geometry at 5 years.

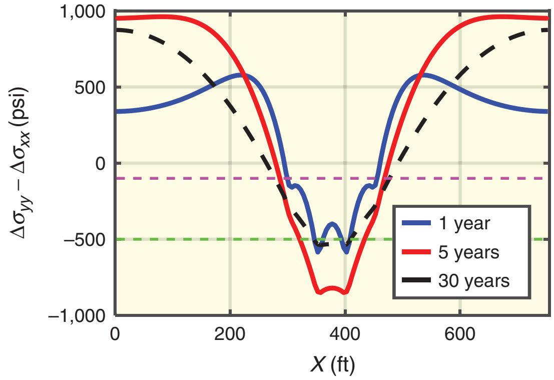

(a) $\Delta\sigma_{yy} - \Delta\sigma_{xx}$ for planar-fracture geometry at different times

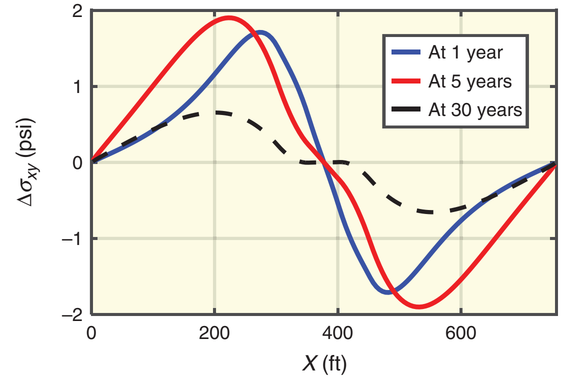

(b) $\Delta\sigma_{xy}$ for planar-fracture geometry at different times

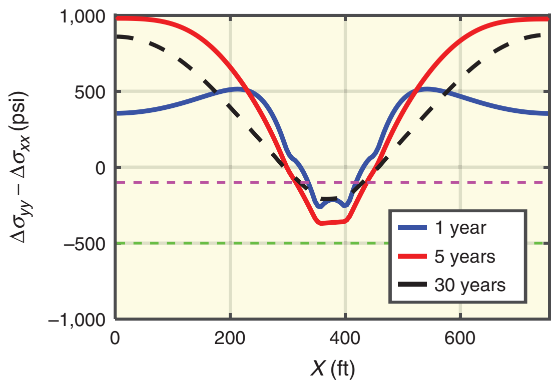

(c) $\Delta\sigma_{yy} - \Delta\sigma_{xx}$ for 60° inclination fracture geometry at different times

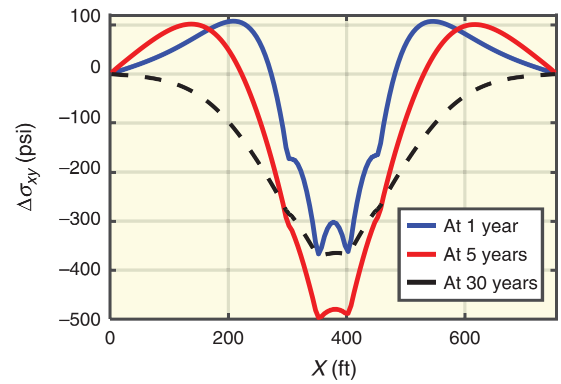

(d) $\Delta\sigma_{xy}$ for 60° inclination fracture geometry at different times

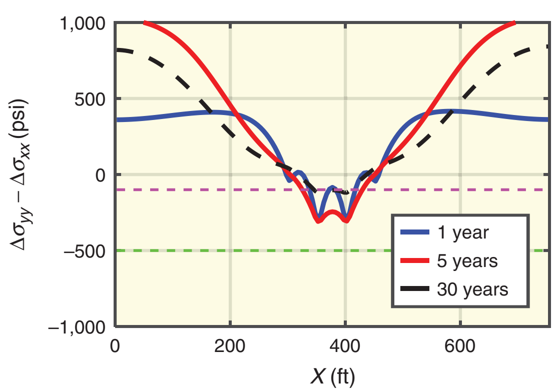

(e) $\Delta\sigma_{yy} - \Delta\sigma_{xx}$ for nonplanar-fracture geometry at different times

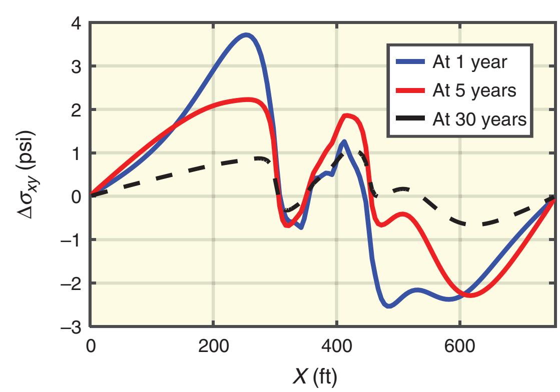

(f) $\Delta\sigma_{xy}$ or nonplanar-fracture geometry at different times

Fig. 15—On the left, change of DS along center of the well for three different geometries (a, c, e) at different times. On the right, shear stress along center of the well for three different geometries (b, d, f) at different times. (a) $\Delta\sigma_{yy}-\Delta\sigma_{xx}$ for planar-fracture geometry at different times; (b) $\Delta\sigma_{xy}$ for planar-fracture geometry at different times; (c) $\Delta\sigma_{yy}-\Delta\sigma_{xx}$ for 60°-inclination fracture geometry at different times; (d) $\Delta\sigma_{xy}$ for 60°-inclination fracture geometry at different times; (e) $\Delta\sigma_{yy}-\Delta\sigma_{xx}$ for nonplanar-fracture geometry at different times; (f) $\Delta\sigma_{xy}$ for nonplanar-fracture geometry at different times.

k_{f2} = permeability inside Fracture Cell 2, md
K_{dr} = drain bulk modulus, psi
K_s = bulk modulus of solid grain, psi
$\overline{\overline{K}}$ = matrix-permeability tensor, md
L = domain length, ft
L_{int} = length of the intersection line, ft
L_x = domain length in x-direction, ft
L_y = domain length in y-direction, ft
L_z = domain length in z-direction, ft
M = Biot modulus, psi
M_f = Biot modulus inside fracture domain, psi
$\vec{n}$ = normal vector of fracture plane, dimensionless
N_x = number of cells in x-direction, dimensionless

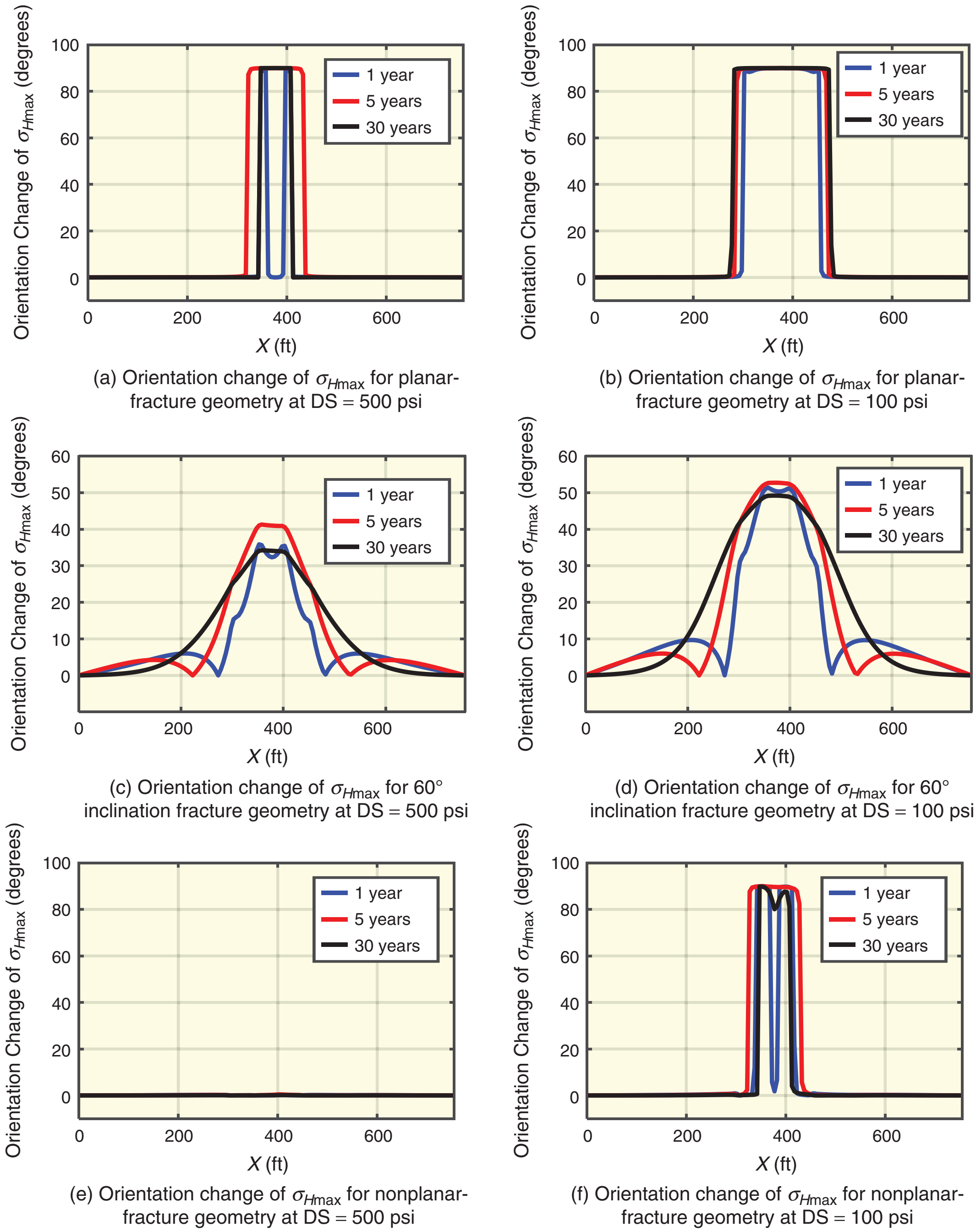

(a) Orientation change of $\sigma_{H\max}$ for planar-fracture geometry at DS = 500 psi

(b) Orientation change of $\sigma_{H\max}$ for planar-fracture geometry at DS = 100 psi

(c) Orientation change of $\sigma_{H\max}$ for 60° inclination fracture geometry at DS = 500 psi

(d) Orientation change of $\sigma_{H\max}$ for 60° inclination fracture geometry at DS = 100 psi

(e) Orientation change of $\sigma_{H\max}$ for nonplanar-fracture geometry at DS = 500 psi

(f) Orientation change of $\sigma_{H\max}$ for nonplanar-fracture geometry at DS = 100 psi

Fig. 16—(a, b) Orientation change along the *x*-direction at y = 377.5 ft for planar-fracture geometry; (c, d) 60°-inclination fracture geometry; and (e, f) nonplanar-fracture geometry at different production times for DS = 100 and 500 psi. (a) Orientation change of $\sigma_{H\max}$ for planar-fracture geometry at DS = 500 psi; (b) orientation change of $\sigma_{H\max}$ for planar-fracture geometry at DS = 100 psi; (c) orientation change of $\sigma_{H\max}$ for 60°-inclination fracture geometry at DS = 500 psi; (d) orientation change of $\sigma_{H\max}$ for 60°-inclination fracture geometry at DS = 100 psi; (e) orientation change of $\sigma_{H\max}$ for nonplanar-fracture geometry at DS = 500 psi; (f) orientation change of $\sigma_{H\max}$ for nonplanar-fracture geometry at DS = 100 psi.

N_y = number of cells in *y*-direction, dimensionless
N_z = number of cells in *z*-direction, dimensionless
p = fluid pressure, psi
p_b = boundary pressure, psi
p_f = pressure of fluid inside fracture domain, psi
p_0 = fluid pressure at initial state, psi
q = source/sink term, s^{-1}
q_{f-m} = flow from fracture domain to matrix domain and vice versa, $ft^3 \cdot s^{-1}$
r_w = well radius, ft
S_{seg} = area of fracture segment perpendicular to the fracture aperture, ft^2
t_d = characteristic time, dimensionless
T = traction force at the boundary, psi
T_{f-f} = transmissibility between two fracture cells, md-ft

T_{f-m} = transmissibility between fracture and matrix cell, md-ft
T_{NNC} = nonneighboring-connections transmissibility, md-ft
T_1 = transmissibility inside Fracture Cell 1, md-ft
T_2 = transmissibility inside Fracture Cell 2, md-ft
u = displacement vector, ft
u_x = displacement in x-direction, ft
u_y = displacement in y-direction, ft
u_z = displacement in z-direction, ft
V = fluid-flow rate, $\text{lbm} \cdot \text{ft}^{-3}$
V_b = bulk volume of the cell assigned to the fracture segment, ft^3
V_c = cell volume, ft^3
V_f = volume of fracture segment, ft^3
w = external load, psi
w_f = fracture width, ft
w_{f1} = fracture width in Cell 1, ft
w_{f2} = fracture width in Cell 2, ft
x = location in x-direction, ft
x_n = distance from fracture cell to matrix cell, ft
y = location in y-direction, ft
z = location in z-direction, ft
Δp = pressure difference between matrix and fracture cell, psi
$\Delta\sigma_{xx}$ = induced stress in x-direction, psi
$\Delta\sigma_{yy}$ = induced stress in y-direction, psi
$\Delta\sigma_{zz}$ = induced stress in z-direction, psi
ε = strain tensor, psi
ε_v = volumetric-strain tensor, psi
λ = first Lamé constant, psi
λ_t = relative mobility, cp^{-1}
μ = second Lamé constant, psi
μ_f = fluid viscosity, cp
ν = Poisson's ratio, dimensionless
ρ_b = single-phase fluid bulk density, $\text{lbm} \cdot \text{ft}^{-3}$
σ = total stress tensor, psi
σ_{eff} = effective stress, psi
$\sigma_{h\text{min}}$ = minimum horizontal stress, psi
$\sigma_{H\text{max}}$ = maximum horizontal stress, psi
σ_v = volumetric mean total stress, psi
$\sigma_{v,0}$ = volumetric mean total stress at initial state, psi
σ_{xx} = total stress in x-direction, psi
$\sigma_{xx,0}$ = initial total stress in x-direction, psi
σ_{yy} = total stress in y-direction, psi
$\sigma_{yy,0}$ = initial total stress in y-direction, psi
σ_{zz} = total stress in z-direction, psi
$\sigma_{zz,0}$ = initial total stress in z-direction, psi
σ_0 = total stress tensor at initial state, psi
τ = coupling strength, dimensionless
ϕ = porosity, dimensionless
ϕ_f = pore volume in fracture cell, dimensionless

Acknowledgments

The authors would like to acknowledge financial support from the Crisman Institute at Texas A&M University.

References

Bai, M. 1999. On Equivalence of Dual-Porosity Poroelastic Parameters. *J. Geophys. Res. Sol. Ea.* **104** (B5): 10461–10466. https://doi.org/10.1029/1999JB900072.

Biot, M. A. 1941. General Theory of Three-Dimensional Consolidation. *J. Appl. Phys.* **12** (2): 155–164. https://doi.org/10.1063/1.1712886.

Biot, M. A. 1955. Theory of Elasticity and Consolidation for a Porous Anisotropic Solid. *J. Appl. Phys.* **26** (2): 182–185. https://doi.org/10.1063/1.1721956.

Cipolla, C. L., Fitzpatrick, T., Williams, M. J. et al. 2011. Seismic-to-Simulation for Unconventional Reservoir Development. Presented at the SPE Reservoir Characterisation and Simulation Conference and Exhibition, Abu Dhabi, 9–11 October. SPE-146876-MS. https://doi.org/10.2118/146876-MS.

Cryer, C. W. 1963. A Comparison of the Three-Dimensional Consolidation Theories of Biot and Terzaghi. *The Quarterly Journal of Mechanics and Applied Mathematics* **16** (4): 401–412. https://doi.org/10.1093/qjmam/16.4.401.

Dean, R. H., Gai, X., Stone, C. M. et al. 2006. A Comparison of Techniques for Coupling Porous Flow and Geomechanics. *SPE J.* **11** (1): 132–140. SPE-79709-PA. https://doi.org/10.2118/79709-PA.

Du, S., Liang, B., and Lin, Y. 2017. Field Study: Embedded Discrete Fracture Modeling With Artificial Intelligence in Permian Basin for Shale Formation. Presented at the SPE Annual Technical Conference and Exhibition, San Antonio, Texas, USA, 9–11 October. SPE-187202-MS. https://doi.org/10.2118/187202-MS.

Gupta, J., Zielonka, M., Albert, R. A. et al. 2012. Integrated Methodology for Optimizing Development of Unconventional Gas Resources. Presented at the SPE Hydraulic Fracturing Technology Conference, The Woodlands, Texas, 6–8 February. SPE-152224-MS. https://doi.org/10.2118/152224-MS.

Jasak, H. and Weller, H. 2000. Finite Volume Methodology for Contact Problems of Linear Elastic Solids. Oral presentation given at the 3rd International Conference of Croatian Society of Mechanics, Cavtat, Croatia.
Jha, B. and Juanes, R. 2014. Coupled Multiphase Flow and Poromechanics: A Computational Model of Pore Pressure Effects on Fault Slip and Earthquake Triggering. *Water Resour. Res.* **50** (5): 3776–3808. https://doi.org/10.1002/2013WR015175.
Kim, J., Tchelepi, H. A., and Juanes, R. 2011a. Stability and Convergence of Sequential Methods for Coupled Flow and Geomechanics: Drained and Undrained Splits. *Comput. Meth. Appl. Mech. Eng.* **200** (23–24): 2094–2116. https://doi.org/10.1016/j.cma.2011.02.011.
Kim, J., Tchelepi, H. A., and Juanes, R. 2011b. Stability and Convergence of Sequential Methods for Coupled Flow and Geomechanics: Fixed-Stress and Fixed-Strain Splits. *Comput. Meth. Appl. Mech. Eng.* **200** (13–16): 1591–1606. https://doi.org/10.1016/j.cma.2010.12.022.
Kim, J., Tchelepi, H. A., and Juanes, R. 2011c. Stability, Accuracy, and Efficiency of Sequential Methods for Coupled Flow and Geomechanics. *SPE J.* **16** (2): 249–262. SPE-119084-PA. https://doi.org/10.2118/119084-PA.
Kim, J., Tchelepi, H. A., and Juanes, R. 2013. Rigorous Coupling of Geomechanics and Multiphase Flow with Strong Capillarity. *SPE J.* **18** (6): 1123–1139. SPE-141268-PA. https://doi.org/10.2118/141268-PA.
Lee, I. S. 2008. *Computational Techniques for Efficient Solution of Discretized Biot's Theory for Fluid Flow in Deformable Porous Media*. PhD dissertation, Virginia Polytechnic Institute and State University, Blacksburg, Virginia.
Li, L. and Lee, S. H. 2008. Efficient Field-Scale Simulation of Black Oil in a Naturally Fractured Reservoir Through Discrete Fracture Networks and Homogenized Media. *SPE Res Eval & Eng* **11** (4): 750–758. SPE-103901-PA. https://doi.org/10.2118/103901-PA.
Mandel, J. 1953. Consolidation des sols (étude mathématique). *Geotechnique* **3** (7): 287–299. https://doi.org/10.1680/geot.1953.3.7.287.
Peaceman, D. W. 1993. Representation Of A Horizontal Well In Numerical Reservoir Simulation. *SPE Advanced Technology Series* **1** (1): 7–16. SPE-21217-PA. https://doi.org/10.2118/21217-PA.
Ren, G., Jiang, J., and Younis, R. M. 2017. Fully-Coupled XFEM-EDFM Hybrid Model for Geomechanics and Flow in Fractured Reservoirs. Presented at the SPE Reservoir Simulation Conference, Montgomery, Texas, 20–22 February. SPE-182726-MS. https://doi.org/10.2118/182726-MS.
Roussel, N. P., Florez, H., and Rodriguez, A. A. 2013. Hydraulic Fracture Propagation from Infill Horizontal Wells. Presented at the SPE Annual Technical Conference and Exhibition, New Orleans, 30 September–2 October. SPE-166503-MS. https://doi.org/10.2118/166503-MS.
Safari, R., Lewis, R., Ma, X. et al. 2015. Fracture Curving Between Tightly Spaced Horizontal Wells. Presented at the Unconventional Resources Technology Conference, San Antonio, Texas, 20–22 July. URTEC-2149893-MS. https://doi.org/10.15530/URTEC-2015-2149893.
Skempton, A. W. 1954. The Pore Pressure Coefficients A and B. *Geotechnique* **4** (4): 143–147. https://doi.org/10.1680/geot.1954.4.4.143.
Tang, T., Hededal, O., and Cardiff, P. 2015. On Finite Volume Method Implementation of Poro-Elasto-Plasticity Soil Model. *Int. J. Numer. Anal. Meth. Geomech.* **39** (13): 1410–1430. https://doi.org/10.1002/nag.2361.
Terzaghi, K. 1925. *Erdbaumechanik auf Bodenphysikalischer Grundlage*. Vienna, Austria: Franz Deuticke.
Wang, B. 2014. *Parallel Simulation of Coupled Flow and Geomechanics in Porous Media*. PhD dissertation, the University of Texas at Austin, Austin, Texas.
Xu, Y. 2015. *Implementation and Application of the Embedded Discrete Fracture Model (EDFM) for Reservoir Simulation in Fractured Reservoirs*. PhD dissertation, the University of Texas at Austin, Austin, Texas.

Appendix A—Analytical Solution of the Terzaghi (1925) and Mandel (1953) Problems

The analytical solutions for pressure (p) and displacement (u_z) at different locations and time can be shown as

$$p(z,t) = -W\frac{a_f - a_i}{\alpha a_i}\sum_{j=0}^{\infty}\frac{4(-1)^j}{\pi(2j+1)}\cos\left[\frac{(2j+1)\pi z}{2H}\right]\exp\left\{-\left[\frac{(2j+1)\pi}{2}\right]^2\frac{c_f t}{4H^2}\right\}, \quad \text{(A-1)}$$

$$u_z(z,t) = -W(a_f - a_i)H\sum_{j=0}^{\infty}\frac{8(-1)^j}{\pi^2(2j+1)^2}\sin\left[\frac{(2j+1)\pi z}{2H}\right]\exp\left\{-\left[\frac{(2j+1)\pi}{2}\right]^2\frac{c_f t}{4H^2}\right\} + Wa_f z, \quad \text{(A-2)}$$

where

$$a_f = \frac{(1+\nu)(1-2\nu)}{E(1-\nu)}, \quad \text{(A-3)}$$

$$a_i = a_f\left(\frac{b^2 a_f}{\phi c_f}\right)^{-1}, \quad \text{(A-4)}$$

where W is the external load on top of the column, H is column height, and z is location along the z-direction.

The analytical solutions for the Mandel (1953) problem for pressure (p) and displacement (u_x and u_y) are written as

$$u_x(x,t) = \left[\frac{W\nu}{2GL} - \frac{W\nu_u}{GL}\sum_{i=1}^{\infty}\frac{\sin\alpha_i\cos\alpha_i}{\alpha_i - \sin\alpha_i\cos\alpha_i}\exp\left(\frac{-\alpha_i{}^2 ct}{L^2}\right)\right]x + \frac{W}{G}\sum_{i=1}^{\alpha}\frac{\cos\alpha_i}{\alpha_i - \sin\alpha_i\cos\alpha_i}\sin\frac{\alpha_i x}{L}\exp\left(\frac{-\alpha_i{}^2 ct}{L^2}\right), \quad \text{(A-5)}$$

$$u_y(y,t) = \left[-\frac{W(1-\nu)}{2GL} + \frac{w(1-\nu_u)}{GL}\sum_{i=1}^{\infty}\frac{\sin\alpha_i\cos\alpha_i}{\alpha_i - \sin\alpha_i\cos\alpha_i}\exp\left(\frac{-\alpha_i{}^2 ct}{L^2}\right)\right]y, \quad \text{(A-6)}$$

where ν_u is the undrained Poisson's ratio, B is the Skempton pore-pressure coefficient, x is the location in the x-direction, y is the location in the y-direction, L is domain length, G is shear modulus, and c is the general consolidation coefficient,

$$c = \frac{2kB^2G(1-\nu)(1+\nu_u)^2}{9(1-\nu_u)(\nu_u - \nu)}. \quad \text{(A-7)}$$

In addition, in Eq. A-6, t is time and α_i, $i = 1, \infty$, are the roots of

$$\tan\alpha_i = \frac{1-\nu}{(\nu_u - \nu)}\alpha_i. \quad \text{(A-8)}$$

In our study, $\nu_u = 0.5$ and $B = \dfrac{1}{(1 + c_f \phi K_{dr})}$. Pressure, total stress σ_{xx}, σ_{yy}, and shear stress σ_{xy} can also be obtained using

$$p(x,t) = \frac{2WB(1+\nu_u)}{3L} \sum_{i=1}^{\infty} \frac{\sin\alpha_i}{\alpha_i - \sin\alpha_i \cos\alpha_i} \left(\cos\frac{\alpha_i x}{L} - \cos\alpha_i \right) \exp\left(\frac{-\alpha_i^2 ct}{L^2} \right), \quad \text{(A-9)}$$

$$\sigma_{xx} = 0. \quad \text{(A-10)}$$

σ_{xx} is zero because of the traction-free boundary on the right of the domain:

$$\sigma_{yy} = \frac{-W}{L} - \frac{2W(\nu_u - \nu)}{L(1-\nu)} \sum_{i=1}^{\infty} \frac{\sin\alpha_i}{\alpha_i - \sin\alpha_i \cos\alpha_i} \cos\frac{\alpha_i x}{L} \exp\left(\frac{-\alpha_i{}^2 ct}{L^2} \right) + \frac{2W}{L} \sum_{i=1}^{\infty} \frac{\sin\alpha_i \cos\alpha_i}{\alpha_i - \sin\alpha_i \cos\alpha_i} \exp\left(\frac{-\alpha_i{}^2 ct}{L^2} \right), \quad \text{(A-11)}$$

$$\sigma_{xy} = 0, \quad \text{(A-12)}$$

because u_y is assumed to be uniform along the x-direction. Thus, σ_{yy} is also uniform along the x-direction. σ_{xy} is zero at all times and external force acts only in the normal direction to the surface. Finally, there is no force acting in the direction parallel to the surface.

SI Metric Conversion Factors

ft × 3.048	E−01 = M
in. × 2.54	E+00 = Cm
psi × 6.895	E+00 = kPa

All conversion factors are exact.

Anusarn Sangnimnuan is a PhD degree candidate in the Harold Vance Department of Petroleum Engineering at Texas A&M University. His research is focused on developing coupled geomechanics/fluid-flow modeling to investigate stress evolution resulting from the depletion effect. Sangnimnuan's work also involves coupling the model with EDFM to predict stress evolution in complex-fracture geometries. He holds bachelor's and master's degrees in mechanical engineering from Chulalongkorn University, Thailand, and the University of Michigan, respectively. Sangnimnuan is a member of SPE.

Jiawei Li is a master's degree student in the Harold Vance Department of Petroleum Engineering at Texas A&M University. His research interests include development of EDFM and application of it to reservoir simulators for complex-fractured reservoirs. Li holds a bachelor's degree in petroleum engineering from China University of Petroleum, East China. He is a member of SPE.

Kan Wu is an assistant professor in the Harold Vance Department of Petroleum Engineering at Texas A&M University. Her research interests include hydraulic fracturing in unconventional reservoirs, coupled geomechanics/fluid-flow modeling, optimization of well performance in unconventional reservoirs, and wellbore strengthening. Wu holds a PhD degree in petroleum engineering from the University of Texas at Austin. She is a member of SPE.